

6-2023

Apatite Reference Materials for SIMS Microanalysis of Isotopes and Trace Elements

James L. Crowley
Boise State University

Mark Schmitz
Boise State University

Publication Information

Kennedy, Allen K.; Wotzlav, Jörn-Frederik; Crowley, James L.; Schmitz, Mark; Schaltegger, Urs; Wade, Benjamin; . . . and Bui, Thi Hao. (2023). "Apatite Reference Materials for SIMS Microanalysis of Isotopes and Trace Elements". *Geostandards and Geoanalytical Research*, 47(2), 373-402. <https://doi.org/10.1111/ggr.12477>

For a complete list of authors, please see the article.

Apatite Reference Materials for SIMS Microanalysis of Isotopes and Trace Elements

Allen K. Kennedy (1)* , Jörn-Frederik Wotzlaw (2, 3), James L. Crowley (4), Mark Schmitz (4), Urs Schaltegger (2), Benjamin Wade (5), Laure Martin (6), Cristina Talavera (7), Bryant Ware (1) and Thi Hao Bui (8)

(1) John de Laeter Centre, Curtin University, Kent. St, Bentley, 6102, Western Australia

(2) Department of Earth Sciences, University of Geneva, Rue des Maraichers 13, CH-1205 Geneva, Switzerland

(3) Department of Earth Sciences, Università degli Studi di Milano, Via Mangiagalli 32, 20133, Milan, Italy

(4) Department of Geosciences, Boise State University, 1910 University Drive, Boise, ID, 83725-1535, USA

(5) Adelaide Microscopy, The University of Adelaide, SA, 5005 Adelaide, Australia

(6) Centre for Microscopy, Characterisation and Analysis, The University of Western Australia, Perth, WA, 6009, Australia

(7) School of Geosciences, University of Edinburgh, The King's Building, James Hutton Road, EH9 3FE Edinburgh, UK

(8) Department of Earth and Planetary Sciences, McGill University, Montreal, Quebec H3A 0E8, Canada

* Corresponding author. e-mail: a.kennedy@curtin.edu.au

Twelve apatite samples have been tested as secondary ion mass spectrometry (SIMS) reference materials. Laser ablation-inductively coupled plasma-mass spectrometry (LA-ICP-MS) analysis shows that the SLAP, NUAN and GR40 apatite gems are internally homogeneous, with most trace element mass fractions having 2 standard deviations (2s) $\leq 2.0\%$. BR2, BR5, OL2, AFG2 and AFB1, which have $U > 63 \mu\text{g g}^{-1}$, $^{206}\text{Pb}/^{204}\text{Pb} > 283$, and homogeneous SIMS U-Pb data, have respective isotope dilution thermal ionisation mass spectrometry (ID-TIMS) ages of $2053.83 \pm 0.21 \text{ Ma}$, $2040.34 \pm 0.09 \text{ Ma}$, $868.87 \pm 0.25 \text{ Ma}$, $478.71 \pm 0.22 \text{ Ma}$ and $473.25 \pm 0.09 \text{ Ma}$. Minor U-Pb heterogeneity exists and accurate SIMS results require correction with the 3D Concordia-constrained common Pb composition. Among the studied samples, AFG2 and BR5 are the most homogeneous U-Pb reference materials. The SIMS sulfur isotopic compositions of eight of the apatites shows they are homogeneous, with 2s for both $10^3\delta^{34}\text{S}$ and $10^3\delta^{33}\text{S} < 0.55\%$. One apatite, BR96, has $\Delta^{33}\text{S} = -0.36 \pm 0.2\%$. The apatite samples have ID-TIMS $^{87}\text{Sr}/^{86}\text{Sr}$ between 0.704214 ± 0.000030 and 0.723134 ± 0.000035 .

Keywords: apatite, SIMS, reference material, U-Pb, O, S, Sr, isotopes.

Received 23 Mar 22 – Accepted 05 Dec 22

Apatite is a fairly ubiquitous mineral and the measurement of apatite trace element mass fractions has provided important constraints on magma crystallisation histories (Tepper and Kuehner 1999, Grange *et al.* 2013, Li *et al.* 2020), ore deposition, and sedimentary, biogenic and metamorphic processes (Wright *et al.* 1987, Bingen *et al.* 1996, Lev *et al.* 1999, Bright *et al.* 2009, Blake *et al.* 2010, Davis *et al.* 2011, Žigaitė and Whitehouse 2014), and the history of fluids and volatiles in terrestrial and extra-terrestrial environments (Ayers and Watson 1993, van Hoose *et al.* 2010, Boyce *et al.* 2014, Hauri *et al.* 2015, Barrett *et al.* 2019).

Apatite is an important mineral in SIMS geochronology with numerous high-profile papers that use apatite U-Pb

systematics to solve critical problems in Lunar, Martian, meteorite and terrestrial evolution (Sano *et al.* 1999, Wiligers *et al.* 2002, Greenwood *et al.* 2003, Storey *et al.* 2007, Davis *et al.* 2011, Li *et al.* 2012, Terada and Sano 2012, Grange *et al.* 2013, Pasek *et al.* 2013, Santos *et al.* 2015, Sano *et al.* 2016, Bellucci *et al.* 2015). SIMS analysis of O, S, and Sr in zircon-hosted apatite is being used to follow the stable isotope evolution of Earth's earliest crust, as well as young volcanic systems (Bruand *et al.* 2017, Yamamoto *et al.* 2017, Boehnke *et al.* 2018, Emo *et al.* 2018, Antione *et al.* 2020, Ravindran *et al.* 2020, Gillespie *et al.* 2021).

Sulfur isotopes provide constraints on ore deposits, S-bearing fluid migration in crustal and surface

doi: 10.1111/ggr.12477

© 2022 The Authors. *Geostandards and Geoanalytical Research* published by John Wiley & Sons Ltd on behalf of the International Association of Geoanalysts.

This is an open access article under the terms of the [Creative Commons Attribution-NonCommercial License](https://creativecommons.org/licenses/by-nc/4.0/), which permits use, distribution and reproduction in any medium, provided the original work is properly cited and is not used for commercial purposes.

environments, mantle source compositions, crustal recycling (Smit *et al.* 2019, Farquhar *et al.* 2002, Giuliani *et al.* 2016) and the evolution of the biosphere and oceans (Johnston 2011). Mass Independent Fractionation (MIF) S isotope signatures have allowed tracking the oxygenation of the Earth's atmosphere in the early Earth (Farquhar *et al.* 2000, Farquhar *et al.* 2003). There are relatively few *in situ* studies of S isotopes in apatite. Even so, SIMS study of apatite has been instrumental in identifying open system behaviour, magma mixing, and changes in fO_2 (Economos *et al.* 2017, Hammerli *et al.* 2021).

Strontium isotopes in apatite allow the tracking of hydrothermal systems in ore deposits (Zhao *et al.* 2015), the study of magma mixing and contamination of silicic and kimberlitic magmas by fluids (Charlier *et al.* 2006, Malarkey *et al.* 2010), the identification of mantle source components (Decree *et al.* 2020), the use of conodont from Palaeozoic to Mesozoic samples to track palaeo-ocean temperatures (Le Houedec *et al.* 2017), and the study of mammalian tooth enamel and bones in palaeontology (Kocsis *et al.* 2021).

SIMS U-Pb and Th-Pb dating of apatite is often limited by large measurement uncertainties associated with small sampling volumes (50–300 μm^3), low mass fractions of U, Th and radiogenic Pb, coupled with higher common Pb contents, and, the necessity to combine the uncertainties of the RM and unknown (Sano *et al.* 2016). Variable major element composition of apatite, with substitution of Cl, F, OH, CO_3 , Mg, Fe, Mn and Si, has the potential to produce matrix induced bias during micro-analysis and thus a collection of RM with known and varying major element compositions is desirable. One of our goals has been to characterise potential apatite RM that have relatively high U, Th and $^{206}\text{Pb}/^{204}\text{Pb}$, so as to reduce the uncertainties associated with SIMS U-Th-Pb analysis. Most apatite is enriched in Th relative to U, and a well-characterised high Th apatite RM would be beneficial for Th-Pb dating of high Th/U hydrothermal apatite in ore deposits (Chen *et al.* 2019).

A large number of apatite have been used as RM for volatile and non-volatile element mass fractions, U-Th-Pb and Lu-Hf geochronology, and isotope ratios of H, O, S, Sr, Cl, and Nd (Sano *et al.* 1999, Amelin and Zaitsev 2002, Horstwood *et al.* 2008, Grange *et al.* 2009, Kennedy 2011, Kennedy *et al.* 2012, Li *et al.* 2012, Barford *et al.* 2005, Chew *et al.* 2011, Marks *et al.* 2012, Thomson *et al.* 2012, Norman and Nemchin 2014, Yang *et al.* 2014, Kusebauch *et al.* 2015, Thompson *et al.* 2016, Silva *et al.* 2018,

Doucance *et al.* 2020, Fisher *et al.* 2020, Gonçalves *et al.* 2020, Yang *et al.* 2020, Gillespie *et al.* 2021, Hammerli *et al.* 2021, Krestianinov *et al.* 2021, Li *et al.* 2021, Simpson *et al.* 2021, Wudarska *et al.* 2021). We have previously distributed BR2 (Grange *et al.* 2009, Nemchin *et al.* 2009, Davis *et al.* 2011, Norman and Nemchin 2014, Bellucci *et al.* 2015) and BR5 (Gall *et al.* 2017, Bao *et al.* 2022), for which there is early U-Pb TIMS data, and the data presented in this article provide an update for the BR2 and BR5 apatite RM.

Inter-laboratory comparison of apatite U-Th-Pb SIMS, ID-TIMS and laser ablation-inductively coupled plasma-mass spectrometry analysis would be facilitated if apatite RMs that have been analysed in multiple ID-TIMS laboratories were available for distribution. Similarly, LA-ICP-MS can benefit from matrix matched RM (Chew *et al.* 2011, Chen and Simonetti 2012, Thompson *et al.* 2016, Fisher *et al.* 2020). Coupled U-Th-Pb ID-TIMS and LA-ICP-MS trace element determination on a single dissolution of an accessory mineral (Schoene *et al.* 2010) requires a RM that is homogenous in both isotopic composition and trace element abundances.

Some of the above listed studies have focused on a single isotope system or a single apatite sample. There is a need for apatite RMs that have been characterised in multiple isotopic systems, as this provides expanded applicability.

Apatite samples

We have chosen not to study biogenic apatite, or apatite with high Cl, CO_3 or OH contents as these substitutions onto specific structural sites in apatite may be associated with bias of SIMS data (Sun *et al.* 2016, Li *et al.* 2021, Wudarska *et al.* 2022). Even though this reduces the applicability of the apatite samples we have characterised, it still provides a set of apatite RMs with compositions that are applicable to a large fraction of igneous, metamorphic and sedimentary apatite.

Although some gem quality apatite, such as those from Durango, show significant chemical variation (Sun *et al.* 2016), we have focused on large, colour-saturated, faceted apatite gems, or large facet-grade crystals of apatite. We have assumed this material is likely to have reduced compositional variability in comparison with apatite grain separates, plus they have very few inclusions, alteration patches and flaws. Twelve facet grade apatite crystals and

faceted apatite gems, purchased from world-wide-web-based gem merchants or mineral dealers, were initially assessed by optical microscopy.

The apatite materials from Campo Formosa (Brazil) are small (0.4–0.8 g), dark royal blue transparent crystals (BR2 and BR5) and a very large (18 g) single crystal (BR96). AFB1 is a dark blue, 1.8 g crystal from Isoanala, Madagascar, and AFG2 is a dark green, 1.5 g crystal, from Fort Dauphin, Madagascar. MADAP is a transparent, neon blue, 0.8 g crystal purchased from a mineral dealer, and Madagascar was given as the source. Apatite from Otter Lake, Quebec, Canada, OL2, OL3, and OL4, are small, grass green, 0.4–0.8 g, flawless, faceted gems. SLAP is a 1 g, flawless, neon blue, faceted gem apatite from Sri Lanka. NUAN and GR40 are dark green, faceted gem apatite with localities given as Nuan Chang, China, and India, and the respective sizes are 1.3 g and 0.3 g. After crushing, with a steel mortar to sub-mm size, any chips with

visible imperfections under a binocular microscope were removed, and any flaws in the mounted chips were avoided during analysis.

Analytical techniques

Optical microscope and secondary electron microscope imaging

Optical, back-scattered electron (BSE), and cathodoluminescence (CL) imaging were completed at the Microscopy and Microanalysis Facility of the John de Laeter Centre, Curtin University. A Nikon SMZ800 stereo-microscope and the associated image analysis software were used for optical imaging. BSE and CL images were produced with a TESCAN MIRA3 variable pressure field emission scanning electron microscope (VP-FESEM), using a 15 kV acceleration potential and a working distance of 14 mm for BSE and 17.5–21.5 mm

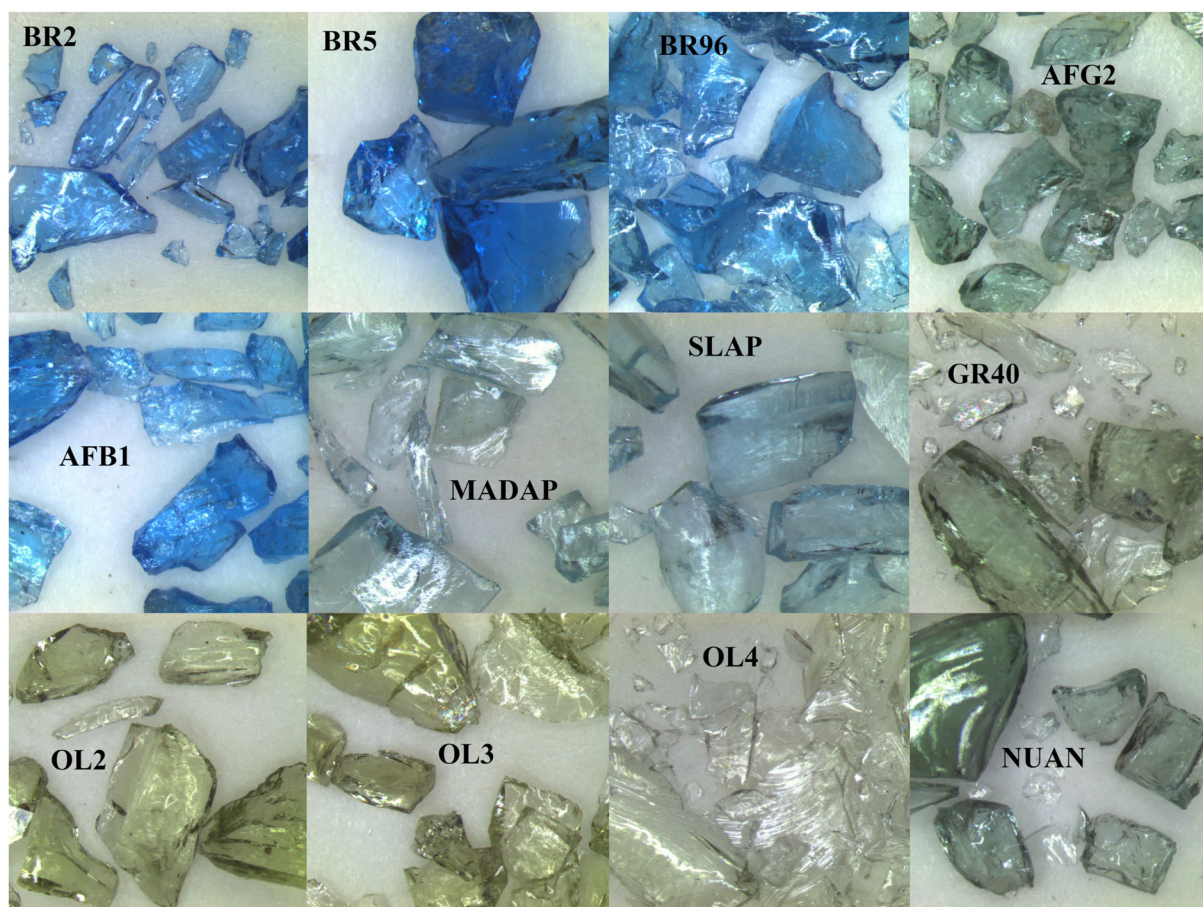


Figure 1. Stereoscopic light images of chips of the characterised apatite showing the colour, transparency and near flawless nature of the faceted gems and facet grade gem crystals. All the images have a 5 cm × 5 cm field of view.

for CL. Stereoscopic images of chips of the apatite samples show that broken chips of the faceted gems and the gem quality crystals are colour-saturated and have excellent clarity (Figure 1). Most of the apatite has minor imperfections, such as feathers and rare micrometre-sized inclusions or altered surfaces of cracks. Chips of the apatite samples were cast in 24 mm diameter epoxy mounts and polished to expose the maximum cross-sectional area, and then cleaned and coated with 40 nm of high purity Au. These mounts were used for all analytical techniques, except TIMS analysis. The CL images of most of the studied apatite exhibit uniform brightness, within and between chips (Figure 2). BR2, BR5, BR96, AFG2, OL2, OL3 and GR40 all have very little CL emission, and this can be seen in Figure 2a. This is likely due to low levels of CL emitting elements, such as the REE, and CL suppression by higher U contents. The CL images of the low U apatite samples, SLAP, MADAP, NUAN and OL4 (Figure 2b–e) were collected at slow scan speeds to counteract the streaking resulting from the long CL emission interval. The CL images for these apatite samples show there is very little heterogeneity. The AFB1 apatite image

(Figure 2b) shows there is minor heterogeneity in CL emission and that AFB1 is not homogenous in CL emitting elements.

Electron probe microanalysis-wavelength dispersive spectrometry (EPMA-WDS)

Quantitative EPMA-WDS analysis of the apatite samples was performed at Adelaide Microscopy at the University of Adelaide, using a Cameca SX Five instrument equipped with five tuneable wavelength-dispersive spectrometers. Fifteen elements were measured following methodologies for apatite data collection/analysis of Nixon *et al.* (2021). Combined analytical conditions of 10 kV/15 nA/5 μ m were used for the measurement of mobile and beam sensitive elements, and 15 kV/40 nA/5 μ m for low-level elements. Both synthetic glasses and natural albite, almandine, apatite, augite, barite, olivine, rhodonite and tugtupite were used as reference materials. Probe for EPMA-WDS software, which uses Mean Atomic Number (MAN) background fitting, and Time Dependant Intensity (TDI) corrections, was utilised for

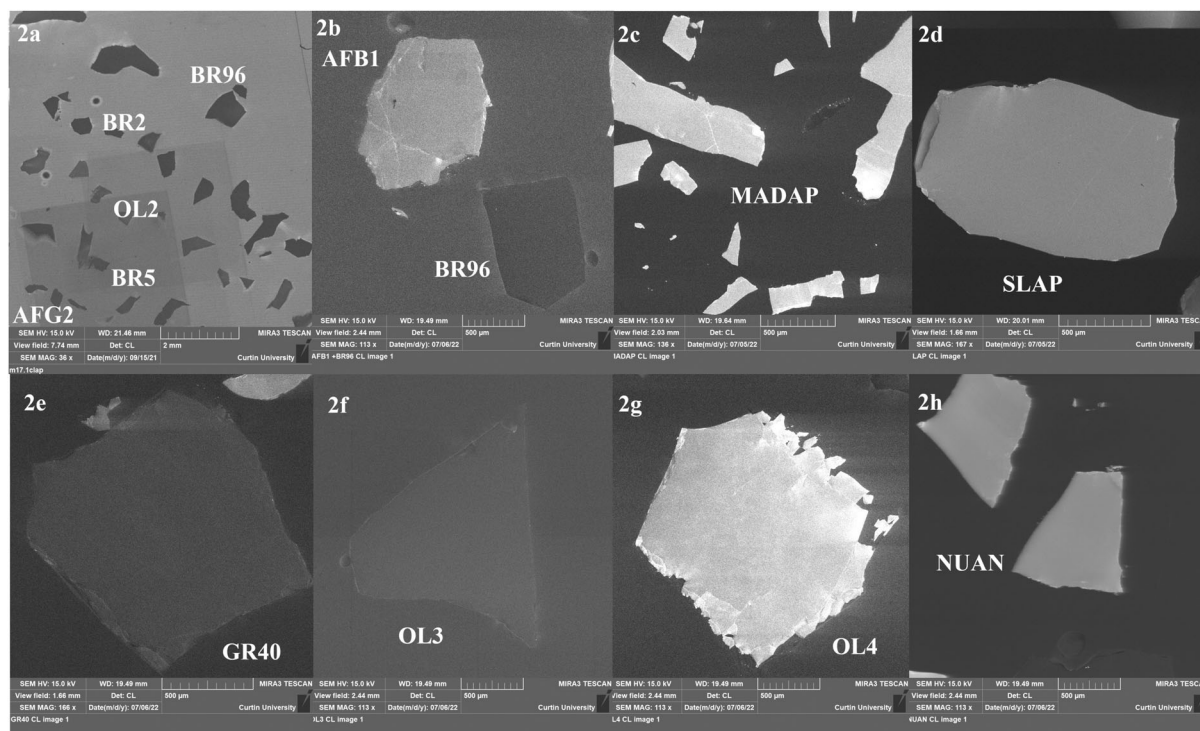


Figure 2. CL images that are representative of the characterised apatite. The cracking of the chips is a result of mounting and polishing and is not intrinsic to the apatite. Image (2a), contains one or more mm-sized chips of the BR2, BR5, BR96 and AFG2 apatite, shows the lack of CL emission for these apatite. None of the chips of the apatite show any visible zonation or compositional variation. The CL images (2b–h) are representative of what was observed for the other apatite, with only AFB1 showing any variation of CL intensity. The scale bar and operating conditions are given at the base of each image.

data acquisition and processing. Detailed information on methodologies, detection limits, overlap corrections and errors can be found in Nixon *et al.* (2021).

LA-ICP-MS trace element measurement

Trace element compositions of multiple fragments of the apatite samples were measured at Adelaide Microscopy (University of Adelaide) using LA-ICP-MS, following the method of Raimondo *et al.* (2011). Analyses were performed on five 1–2 mm chips of each apatite that were mounted in a 24 mm diameter epoxy disk, and analysed with an Agilent 7500cs quadrupole ICP-MS equipped with a New Wave UP-213 Nd-YAG laser. Beam diameter was set at 30 μm , with a repetition rate of 5 Hz and energy set to produce a fluence at the sample of $\sim 9\text{--}10 \text{ J cm}^{-2}$. Ablation was conducted in a helium atmosphere after which argon gas added immediately after the cell to aid transport of material. The instrument was tuned to optimum sensitivity and to minimise production of interfering oxides species, with $^{232}\text{Th}^{16}\text{O}/^{232}\text{Th}$ routinely $< 0.5\%$. Data was collected using time-resolved data acquisition in fast peak-jumping mode and processed using the Lolite software (Paton *et al.* 2011). Total acquisition time per analysis was 80 s, with 40 s background measurement followed by 40 s of sample ablation. Calibration was performed against the NIST SRM 610 glass using the coefficients of Pearce *et al.* (1997). Batches of ten analyses were bracketed by repeat analyses of the reference material NIST SRM 610, allowing monitoring of, and correction for, instrumental drift. A linear drift correction based on the analysis sequence and on the bracketing analyses of NIST SRM 610, was applied to the count rate for each sample. In addition to this, analyses of USGS basalt glasses BHVO and BCR were also analysed to monitor for bias. ^{43}Ca was used as the internal standard element for each apatite analysis, using the EPMA-WDS value for Ca in each apatite grain. The precision of trace element measurements, based on repeated analyses of RMs, is approximately $\pm 10\%$ for mass fractions $< 10 \mu\text{g g}^{-1}$. The detection limits for Li, Cl, Nb, Hf, Ta and W are $< 10 \mu\text{g g}^{-1}$, for Ca $< 200 \mu\text{g g}^{-1}$ and for Si $< 900 \mu\text{g g}^{-1}$. Typical detection limits for Sr and elements with mass > 92 ranged from 0.015 to 0.09 $\mu\text{g g}^{-1}$. For some apatite samples there are only four analyses and additional work is needed to fully assess their homogeneity.

SIMS U-Th-Pb

The U-Th-Pb analytical procedures for the Curtin consortium Sensitive High Resolution Ion Micro-Probe (SHRIMP) have been described by de Laeter and Kennedy (1998)

and Kennedy *et al.* (2012) and are similar to those described by Compston *et al.* (1984), Williams (1998), Ireland and Williams (2003) and Kennedy *et al.* (2010, 2014). Typically, a 25–30 μm diameter spot was used, with a mass-filtered O_2^- primary beam of 2–3 nA. Data for each spot were collected in sets of six scans through twelve mass stations corresponding to $^{44}\text{Ca}^{40}\text{Ca}^{31}\text{P}^{16}\text{O}_4^+$, $^{197}\text{Au}^+$, $^{204}\text{Pb}^+$, Background, $^{206}\text{Pb}^+$, $^{207}\text{Pb}^+$, $^{208}\text{Pb}^+$, $^{208}\text{Pb}^{1}\text{H}^+$, $^{232}\text{Th}^{16}\text{O}^+$, $^{238}\text{U}^{16}\text{O}^+$, $^{232}\text{Th}^{16}\text{O}_2^+$ and $^{238}\text{U}^{16}\text{O}_2^+$, with respective count intervals of 4, 2, 40, 30, 40, 30, 10, 5, 5, 10, 5 and 10 seconds. The SIMS $^{206}\text{Pb}/^{238}\text{U}$ ages were calculated using one of the apatite for calibration, along with the measured TIMS age for this apatite. The common Pb correction for BR2, BR5, AFG2 and OL2 uses the measured $^{204}\text{Pb}/^{206}\text{Pb}$ ratio and the common Pb composition calculated from the concordia constrained TIMS 3D linear regression. Instrumental Mass Fractionation (IMF) was monitored using the $^{207}\text{Pb}/^{206}\text{Pb}$ ratio of NIST SRM 610 glass or Broken Hill Pb feldspar (Stern *et al.* 2009). Correction for common Pb for the AFB1 apatite is complicated by the presence of an unidentified interference on the ^{204}Pb that is similar to that seen in monazite (Stern and Berman 2001). This necessitated the use of the ^{207}Pb correction scheme of Compston *et al.* (1984). Figure 3 shows the difference in the calculated age for AFB1 using a ^{204}Pb or ^{207}Pb common Pb correction for a single data set. AFB1 is the only apatite with an identifiable interference on ^{204}Pb .

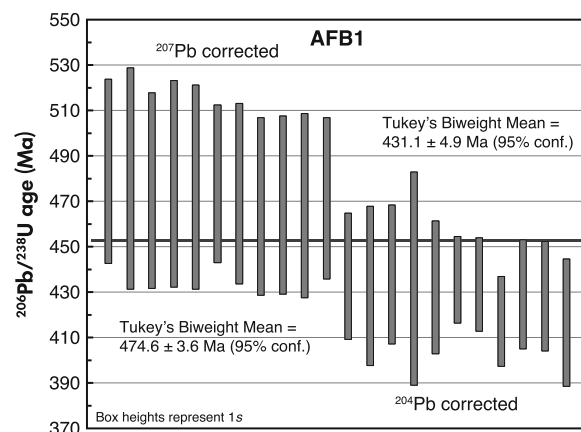


Figure 3. Tukey's biweight mean $^{206}\text{Pb}/^{238}\text{U}$ age for the AFB1 apatite using the ^{204}Pb and ^{207}Pb common Pb correction methods (Compston *et al.* 1984) for a single SHRIMP analytical data set. The consistently younger ^{204}Pb corrected ages can be attributed to a possible Th molecular species ion interference at the ^{204}Pb mass.

The correction formula for Pb/U fractionation is $^{206}\text{Pb}^+ / ^{238}\text{U}^{16}\text{O}^+ = a(^{238}\text{U}^{16}\text{O}_2^+ / ^{238}\text{U}^{16}\text{O}^+)^b$, which is similar to the approach of Clauoué-Long *et al.* (1995), but replacing $^{238}\text{U}^+$ by $^{238}\text{U}^{16}\text{O}^+$ and $^{238}\text{U}^{16}\text{O}^+$ by $^{238}\text{U}^{16}\text{O}_2^+$. The calibration constant for Pb/Th uses $^{208}\text{Pb}^+ / ^{232}\text{Th}^{16}\text{O}^+ = a(^{232}\text{Th}^{16}\text{O}_2^+ / ^{232}\text{Th}^{16}\text{O}^+)^b$. The calculated ages and concordia diagrams use the decay constants of Jaffey *et al.* (1971). The programs Isoplot and SQUID II (Ludwig 2003, 2009), SQUID 3 (Bodorkis *et al.* 2020) and IsoplotR (Vermeesch 2018) were used for data processing and plotting.

U-Pb isotope dilution thermal ionisation mass spectrometry (ID-TIMS)

The U-Pb ID-TIMS ages of five of the potential apatite reference materials were determined in the geochronology laboratories at Boise State University (BSU) and the Department of Earth Sciences of the University of Geneva (UNIGE). Procedures employed at BSU and UNIGE follow those described by Schoene *et al.* (2010) and Wotzlav *et al.* (2012).

Apatite chips were selected and transferred to 3 ml Teflon PFA beakers with ultrapure H₂O and ultrasonically cleaned. The grains were rinsed with ultrapure H₂O before being transferred to 200 µl Savillex PFA microcapsules, spiked with the EARTHTIME mixed (²⁰²Pb-²⁰⁵Pb-²³³U-²³⁵U) tracer solution (ET(2)535) (<http://www.earth-time.org/>) and dissolved in 6 mol l⁻¹ HCl in Parr bombs at 180 °C. U and Pb were separated using a HBr- and HCl-based anion exchange chromatographic procedure (Krogh 1973). The Pb and U fractions were loaded separately on single out-gassed Re filament with ~1 µl of a silica gel/phosphoric acid mixture modified from Gerstenberger and Haase (1997). U and Pb isotopic measurements made on a GV Isoprobe-T multi-collector thermal ionisation mass spectrometer equipped with an ion-counting Daly detector at BSU and a Thermo TRITON thermal ionisation mass spectrometer equipped with a MasCom secondary electron multiplier at UNIGE. At BSU Pb isotopes were measured by peak jumping all isotopes on the Daly detector for 100 to 150 cycles. At UNIGE Pb isotopes were either measured by dynamic peak hopping on the axial multiplier or in static mode on Faraday cups equipped with 10¹² Ω resistors. At BSU Pb isotopes were corrected for 0.22 ± 0.04% per amu (atomic mass unit) mass fractionation. At UNIGE Pb isotopes were corrected using a fractionation factor derived from the measured ²⁰²Pb/²⁰⁵Pb ratio assuming a true value of 0.99924 for the tracer. In both laboratories, uranium was determined as UO₂⁺ ions in static Faraday mode on 10¹¹ or 10¹² Ω resistors for 150 to 200 cycles, and corrected for

isobaric interference of ²³³U¹⁸O¹⁶O on ²³⁵U¹⁶O¹⁶O with an ¹⁸O/¹⁶O of 0.00205 and for mass fractionation using the measured ²³³U/²³⁵U ratio relative to a value of 0.99506 for the ET (2)535 tracer. U-Th-Pb dates and uncertainties were calculated using the algorithms of Schmitz and Schoene (2007) and using the U decay constants of Jaffey *et al.* (1971). The common Pb in the analyses was attributed to initial Pb, ignoring the insignificant contribution from the laboratory blank, and corrected using the Pb isotopic composition and associated uncertainty calculated from the 3D total Pb isochron solution from Isoplot, using all analyses from both laboratories. The data has not been corrected for initial ²³⁰Th disequilibrium. All uncertainties are reported at the 95% confidence level and exclude systematic uncertainties associated with tracer calibration and decay constants unless otherwise indicated.

Gas-source S isotope ratio mass spectrometric analysis of apatite

Each apatite sample was dissolved in Thode solution (mixture of (32:15:53) HI, H₃PO₂ and HCl) at 100 °C under a stream of pure N₂ for 90 min (Thode *et al.* 1961). The N₂ carried the generated H₂S through a zinc acetate solution, which quantitatively precipitated the H₂S as ZnS. A few drops of silver nitrate (0.1 mol l⁻¹) were added to the zinc acetate solution to convert the ZnS to Ag₂S. This reaction was carried out overnight in the dark. The Ag₂S was then separated from the solution by filtration on a 0.2 µm membrane filter, rinsed with a few millilitres of ammonium hydroxide and three times with high-purity (Milli-Q) water, scraped from the filter, and dried for > 24 h at 50 °C. The samples were then weighed to evaluate recovery relative to the starting mass of each apatite sample, which was typically 30 mg. Typical recoveries were > 90% S. We view these as acceptable recoveries given the potential losses in manipulating such small quantities of solids.

The Ag₂S was reacted in the presence of excess fluorine gas for 12 h in a Ni reaction vessel heated to 250 °C. The SF₆ generated by the reaction was first purified by removing non-condensable by-products of the reaction by cryo-separation at -120 °C. A second purification was carried out by passing the SF₆ through two GC columns (~ 2 m Haysep Q and ~ 2 m Molsieve 5A) with ultrapure He as the carrier gas at a rate of 20 ml min⁻¹. The SF₆ peak was isolated from residual contaminants and the carrier gas by trapping the SF₆ on a cold finger at -192 °C as the carrier gas was pumped out. The isotopic composition of the purified SF₆ was then determined on a ThermoElectron MAT 253 dual Inlet isotope ratio mass spectrometer in the Stable

Isotope Laboratory of the Earth and Planetary Sciences
Department at McGill University.

SIMS sulfur isotope measurements

Sulfur isotope (^{32}S , ^{33}S and ^{34}S) measurements were performed using a CAMECA IMS1280 instrument at the Centre for Microscopy and Characterisation and Analysis (CMCA), University of Western Australia. The S isotope SIMS technique of Hammerli *et al.* (2021) was used as the basis for our technique, with minor adjustments. We used 25 mm epoxy mounts in a standard CAMECA holder with the Big, Durango-A, SAP1 RM apatites in one mount and large chips of the apatite being characterised in a second mount. The apatite samples were centrally located to reduce any edge effect (Ickert *et al.* 2008, Kita *et al.* 2011). Normal incident electrons were used for charge compensation during analysis. Epoxy resin mounts were carefully cleaned with detergent, ethanol and distilled water and then coated with 20 nm-thick Au. Each analysis included pre-sputtering over a $20\ \mu\text{m} \times 20\ \mu\text{m}$ area for 60 s and the automatic centring of the secondary ions in the field aperture. During data collection the sample surface was sputtered over a $15\ \mu\text{m} \times 15\ \mu\text{m}$ area with a 10 kV, Gaussian Cs^+ beam with intensity of $\sim 1\text{--}3\ \text{nA}$ and total impact energy of 20 keV. Secondary S^- ions were admitted to the double focusing mass spectrometer within a 90- μm entrance slit and focused in the centre of a 3000 μm field aperture ($\times 130$ magnification). Energy filtering was applied using a 30 eV band pass with a 5 eV gap toward the high-energy side. The isotopes ^{32}S , ^{33}S and ^{34}S were simultaneously measured in multi-collection mode with one Faraday Cup using amplifiers with $10^{11}\ \Omega$ (L1), and two low-noise ion counting electron multipliers (C and H2). Multi-collection detectors operated at a mass resolution of ~ 4300 , which is sufficient to resolve isobaric interferences on ^{32}S from $^{31}\text{P}^1\text{H}$ and on ^{33}S from $^{32}\text{S}^1\text{H}$. The magnetic field was regulated using NMR control. Each analysis then consisted of thirty 4 s acquisition periods. For the isotope homogeneity test of potential RMs, the stability of the instrument and “external” precision were monitored using a restricted area ($\sim 200\ \mu\text{m} \times 100\ \mu\text{m}$) within a single grain of apatite and by repeating the measurements in this area every five to ten analyses, which targeted other areas of the grain. For measuring bias, we used our apatite samples with gas source bulk S isotope composition, SLAP and AFG2, to correct for drift, monitor “external” reference material reproducibility and correct for IMF. When present, instrumental drift was corrected via linear functions (Hammerli *et al.* 2021).

TIMS Sr isotope measurement

Strontium isotope ratios were determined by thermal ionisation mass spectrometry (TIMS) on a Thermo Fisher TritonTM instrument at the John de Laeter Centre (JdLC) at Curtin University in Perth, Western Australia. Eleven apatite powder test portions of 10–35 mg were processed for Sr isotopic measurements. After each test portion was weighed, digestion occurred using concentrated ($16\ \text{mol l}^{-1}$) HNO_3 within capped PTFE beakers on a hot plate at 120 °C for 48 h. Once all had been completely digested, they were evaporated and then twice dissolved in $6\ \text{mol l}^{-1}$ HCl to transform the nitrate to chloride. Lastly, the samples were dissolved in 1 ml of $2.5\ \text{mol l}^{-1}$ HCl in preparation for chromatography. Purification of the Sr was accomplished by passing the solution through a cation resin exchange column packed with Bio-Rad AG50W-X8. The quartz column was cleaned prior to chemistry with 25.0 ml $6\ \text{mol l}^{-1}$ HCl. After pre-cleaning and prior to sample introduction the resin was conditioned in 2.0 ml of $2.5\ \text{mol l}^{-1}$ HCl. The 1 ml of sample solution was carefully introduced into each respective column. The resin loaded with the sample was then washed twice with 2.5 ml of $2.5\ \text{mol l}^{-1}$ HCl, followed by 2.5 ml of $5\ \text{mol l}^{-1}$ HCl to remove all unwanted matrix elements. The Sr fraction was collected using 3.5 ml of $5\ \text{mol l}^{-1}$ HCl and subsequently dried on the hotplate. Each sample was then dissolved twice in 250 μl of $8\ \text{mol l}^{-1}$ HNO_3 , placed in an ultrasonic bath, evaporated before being dissolved in 1 ml of ultra pure $8\ \text{mol l}^{-1}$ HNO_3 for final purification. To be sure of complete Sr purification, the Sr separation sample solution was loaded into columns filled with Eichrom Sr resin (50–100 μm size) that had been pre-cleaned in high-purity water. Any remaining matrix elements were removed by repetitive ($\times 3$) introduction of $8\ \text{mol l}^{-1}$ HNO_3 . Collection of the Sr was accomplished by elution with 2 ml of high-purity water (Milli-Q) and subsequent drying on a hot plate with 2.5 μl of H_3PO_4 . The Sr fractions were evaporated and redissolved in 2.5 μl $16\ \text{mol l}^{-1}$ HNO_3 prior to mass spectrometry.

The purified and dried Sr sample was redissolved in ultra pure 5.0 μl of $6\ \text{mol l}^{-1}$ HNO_3 , from which 1 μl of the sample solution was mixed with 1 μl TaF_5 activator and loaded onto the centre of pre-outgassed single Re filament. After being allowed to dry on the filament at a 0.8 A current, the samples were ready for analysis. The Sr isotopic ratios were acquired in the static collection mode on Faraday cups using a $1 \times 10^{11}\ \Omega$ resistors. Gain calibration bias and amplifier gains were calibrated at the start of each day's measurement session. Prior to each measurement the filaments were heated to ca. 1250 °C (2000 mA) and left

for 2 min to further confirm the complete removal of Rb to avoid any isobaric overlap of ^{87}Rb on ^{87}Sr . Measurement of the Sr isotopes were conducted with a filament temperature of 1350–1450 °C after a slow heating and beam tuning protocol. Once a stable signal was acquired each filament was analysed twice using a method consisting of ten blocks of ten scans at two differing temperatures. The isobaric interference of ^{87}Rb on ^{87}Sr was monitored during the Sr measurements using ^{85}Rb . The ^{85}Rb signal was at the baseline noise of the amplifier throughout the analytical run and thus the Rb interference was determined to be negligible during the entire analysis resulting in no need for any correction. The $^{87}\text{Sr}/^{86}\text{Sr}$ ratio data were corrected for mass fractionation by normalising to an $^{86}\text{Sr}/^{88}\text{Sr}$ ratio of 0.1194 using the exponential law.

The NIST SRM 987 reference material was analysed a number of times throughout the measurement session at the beginning, mid-way through the samples, and at the end. The reference material was used to evaluate the instrument stability during the measurement session over the multiple days of analyses. Furthermore, to be sure no fractionation was induced during chemical processing an aliquot of NIST SRM 987 was processed along with the sample material. The measured mean value of the NIST SRM 987 was 0.710238 ± 0.00002 (2s, $n = 7$) for $^{87}\text{Sr}/^{86}\text{Sr}$, in excellent agreement with the reported certified ratio of 0.710250.

Results and discussion

EPMA-WDS

Electron probe-WDS measurements were undertaken on five to ten chips of each apatite sample. The normalised weighted mean mass fractions are given in Table 1. Our EPMA-WDS analyses resulted in totals between 98.9 in AFB1 and 100.18 g/100g in MADAP, after correction for F and Cl substitution for O. The shortfall in mass is likely to be a reflection of the presence of OH, CO_3 and additional trace constituents in the apatite structure, and movement of F under the electron beam. Sodium, Mg, Fe and Mn were absent or present at very low levels in all apatite samples. There are small differences in S, Cl, F, Si, Y and trace elements between the apatite samples. OL2 and OL3 have higher trace element abundances and S than OL4, the other Otter Lake apatite specimen. All of the apatite samples studied had typical fluorapatite compositions with F between 2.6% in NUAN and 4.1% in OL4. OL2, OL3 and OL4 returned F mass fractions greater than the structural limit for apatite ($\sim 3.77\%$ m/m). The Time Dependant Intensity (TDI) plots of F

for these samples display convoluted time resolved signals, and this is seen to reflect the migration of F due to c-axis orientation effects of the mounted apatite grains. Despite this, the absence of measurable Cl and good totals suggests that they are at, or close to, the fluorapatite end member composition. The WDS data for the apatite samples lets us conclude that there is a limited range of compositions for all major and minor elements measured by WDS, and that there is nothing unusual about the composition of the different apatite samples. Although some trace element mass fractions were measured by WDS we will discuss the variation of trace elements within the apatite samples in the following section.

LA-ICP-MS

The apatite trace element data given in Table 2 were measured on the same apatite chips as the WDS analyses. There is a large range in the weighted and unweighted mean abundance of trace elements between the different apatite samples. For example, La contents range from $200 \mu\text{g g}^{-1}$ to $2740 \mu\text{g g}^{-1}$, Sr ranges between 260 and $3601 \mu\text{g g}^{-1}$, Th between 9.3 and $5180 \mu\text{g g}^{-1}$ and Y between 123 and $1005 \mu\text{g g}^{-1}$.

As a consequence, the chondrite normalised (C.N.) Rare Earth Element (REE) patterns, plotted in Figures 4a and b show orders of magnitude variation. The apatite from Brazil, Madagascar and Sri Lanka (Figure 4a), all have typical apatite REE patterns, with LREE enrichment, a negative Eu anomaly, a smooth curvature to the LREE and HREE patterns, and REE abundances typical of apatite from granitic rocks and pegmatite (Belousova *et al.* 2002). In Figure 4b, only NUAN has a different REE pattern to the other apatite samples, with a pattern that is often associated with ultramafic rocks and iron-apatite ores (Belousova *et al.* 2002). NUAN has a relatively flat REE pattern, a small Eu anomaly, and a small enrichment of Yb and Lu over the other HREE.

Additional trace element data are given in Table 2. SLAP, GR40 and NUAN have good trace element homogeneity, with 2s for all the REE being $< 2.3\%$. OL2 and OL3 have higher Y than the remainder of the apatite samples, and this is consistent with their higher HREE. The BR apatites have lower Y and Zr. The Th abundance of the analysed apatite samples is highly variable, ranging from $5180 \mu\text{g g}^{-1}$ in AFB1 to $9.3 \mu\text{g g}^{-1}$ in NUAN. Uranium has a much narrower range, varying from 24 to $144 \mu\text{g g}^{-1}$. Lead is present in all of the apatite samples examined, and the approximate abundance ranges from $9.4 \mu\text{g g}^{-1}$ in NUAN to $123 \mu\text{g g}^{-1}$ in AFB1.

Table 1.
Measurement results for major and trace elements in apatite reference samples by EPMA

Element	BR2	2SE (n = 12)	BR5	2SE (n = 9)	BR96	2SE (n = 13)	AFG2	2SE (n = 17)	AFB1	2SE (n = 14)	MADAP	2SE (n = 13)
	Mass%		Mass%		Mass%		Mass%		Mass%		Mass%	
F	3.00	0.13	2.39	0.05	2.89	0.04	3.50	0.06	3.82	0.10	3.54	0.04
Na ₂ O	0.07	0.01	0.10	0.02	0.15	0.03	0.12	0.03	0.033	0.005	0.17	0.02
MgO	0.02	0.004	0.01	0.003	b.d.l.		b.d.l.		0.002	0.002	b.d.l.	
SrO	0.06	0.004	0.05	0.01	0.04	0.002	0.07	0.004	0.07	0.01	0.26	0.003
SiO ₂	0.93	0.02	0.82	0.05	0.81	0.01	1.23	0.01	1.76	0.01	0.86	0.01
P ₂ O ₅	39.52	0.25	40.58	0.20	40.59	0.25	39.29	0.22	38.06	0.10	40.22	0.13
Y ₂ O ₃	0.02	0.01	0.02	0.01	0.06	0.01	0.05	0.005	0.05	0.01	0.05	0.01
SO ₃	1.11	0.04	0.87	0.03	0.87	0.03	1.23	0.05	1.12	0.01	0.69	0.03
Cl	0.18	0.01	0.23	0.004	0.12	0.02	0.12	0.01	0.14	0.004	0.16	0.01
CaO	55.09	0.24	54.49	0.24	55.29	0.26	55.23	0.29	53.56	0.13	54.82	0.32
La ₂ O ₃	0.04	0.01	0.12	0.07	0.03	0.004	0.10	0.01	0.28	0.05	0.25	0.01
Ce ₂ O ₃	0.08	0.01	0.22	0.08	0.06	0.01	0.26	0.01	0.68	0.05	0.49	0.01
Nd ₂ O ₃	0.06	0.02	0.09	0.05	0.05	0.01	0.09	0.01	0.20	0.03	0.18	0.01
MnO	0.05	0.01	0.03	0.01	0.04	0.003	b.d.l.		0.07	0.01	0.03	0.01
FeO	0.002	0.002	0.01	0.01	0.04	0.01	0.04	0.01	0.02	0.01	0.03	0.002
Total	100.24	0.23	100.02	0.28	100.94	0.42	101.30	0.47	99.85	0.31	101.69	0.28
O ≡ F	1.29	0.03	1.02	0.02	1.25	0.02	1.50	0.03	1.63	0.04	1.53	0.02
O ≡ Cl	0.04	0.01	0.05	0.004	0.03	0.02	0.03	0.01	0.03	0.004	0.04	0.01
Total	98.91	0.20	98.95	0.27	99.70	0.42	99.79	0.46	98.19	0.28	100.15	0.28

Element	OL2 *	2SE (n = 9)	OL3 *	2SE (n = 20)	OL4 *	2SE (n = 12)	GR40	2SE (n = 10)	NUAN	2SE (n = 30)	SLAP	2SE (n = 10)
	Mass%		Mass%		Mass%		Mass%		Mass%		Mass%	
F	4.02	0.16	4.01	0.10	4.12	0.06	3.66	0.06	2.63	0.05	3.60	0.05
Na ₂ O	0.08	0.03	0.18	0.01	0.36	0.05	0.17	0.02	0.13	0.02	0.07	0.01
MgO	0.01	0.01	b.d.l.									
SrO	0.18	0.03	0.19	0.004	0.39	0.01	0.20	0.005	0.03	0.002	0.22	0.003
SiO ₂	1.01	0.15	0.94	0.01	0.07	0.01	0.87	0.01	b.d.l.		0.90	0.01
P ₂ O ₅	39.40	0.55	39.51	0.20	41.99	0.26	40.35	0.32	42.57	0.14	40.24	0.12
Y ₂ O ₃	0.12	0.02	0.16	0.02	0.04	0.01	0.04	0.01	0.05	0.004	0.06	0.01
SO ₃	0.51	0.05	0.49	0.03	0.23	0.01	0.67	0.04	0.13	0.01	0.87	0.02
Cl	0.06	0.08	0.04	0.004	b.d.l.		0.13	0.01	0.07	0.004	0.16	0.01
CaO	53.56	0.28	54.26	0.26	54.44	0.63	54.94	0.53	55.39	0.29	54.31	0.26
La ₂ O ₃	0.33	0.06	0.32	0.01	0.14	0.01	0.23	0.01	0.03	0.001	0.25	0.01
Ce ₂ O ₃	0.91	0.10	0.85	0.01	0.32	0.02	0.47	0.01	0.05	0.004	0.50	0.01
Nd ₂ O ₃	0.38	0.04	0.40	0.01	0.15	0.02	0.17	0.01	0.05	0.004	0.18	0.01
MnO	0.02	0.01	0.02	0.002	0.02	0.003	0.03	0.002	0.17	0.005	0.03	0.004
FeO	0.01	0.01	0.05	0.01	0.04	0.01	0.03	0.01	0.05	0.01	0.04	0.01
Total	100.59	0.57	101.40	0.28	102.27	0.61	101.94	0.64	101.26	0.33	101.41	0.27
O ≡ F	1.72	0.07	1.69	0.04	1.74	0.03	1.57	0.03	1.13	0.02	1.55	0.02
O ≡ Cl	0.01	0.02	0.01	0.004			0.03	0.010	0.02	0.004	0.04	0.01
Total	98.86	0.55	99.71	0.29	100.55	0.61	100.35	0.65	100.15	0.34	99.83	0.26

* F measurements noisy due to F migration under the electron beam

ID-TIMS U-Pb

ID-TIMS U-Pb analysis was completed on five apatite materials (BR2, BR5, AFB1, AFG2 and OL2), which had U > 65 µg g⁻¹ and masses between 0.4 and 1.5 g. The ID-TIMS data for these apatites is given in Table 3. and plotted on Pb-Pb isochron, isotope ratio and Concordia diagrams (Figures 5, 6, 7 and 8). The TIMS data shows that all of the analysed chips contain common Pb. The mole

percentage of radiogenic ²⁰⁶Pb varies between 89% and 99% in individual chips. This is reflected in the relatively high ²⁰⁶Pb/²⁰⁴Pb of the ID-TIMS analysed apatite. The mean TIMS ²⁰⁶Pb/²⁰⁴Pb values for BR2, BR5, AFG2, AFB1 and OL2 are respectively, 561, 948, 323, 283 and 538 (Table 3). All of the analyses of the apatite samples (Tables 3 and 4) have significant amounts of common Pb and the analytical points plot far from the Concordia curve (Figure 5); the calculated ages are highly sensitive to the assumed

Table 2.
Major and trace element data for apatite reference samples by LA-ICP-MS

Element	BR2		BR5		BR96		AFG2		AFB1		MADAP	
	Wtd Mean	2s (%) (n = 4)	Wtd Mean	2s (%) (n = 10)	Wtd Mean	2s (%) (n = 6)	Wtd Mean	2s (%) (n = 4)	Wtd Mean	2s (%) (n = 4)	Wtd Mean	2s (%) (n = 4)
Li	0.05	40.7	Below LOD		6.17	2.6	2.25	5.4	0.20	16.9	0.45	10.9
Si	5143.34	2.5	4279.80	0.82	5118.86	2.3	6445.35	2.5	8688.21	1.9	5601.38	2.9
P	256469	1.1	207214	0.59	238890	0.9	227790	1.1	213038	1.1	222175	1.5
Fe	170.79	2.1	32.77	6.40	200.99	1.6	190.71	1.9	185.55	2.0	183.52	2.1
Sr	366.83	0.8	408.69	0.49	260.47	0.7	456.16	0.8	580.39	0.9	2220.75	0.8
Y	122.89	1.0	324.22	0.52	127.97	1.0	281.23	0.8	435.14	0.9	310.17	1.2
Zr	16.81	1.9	18.66	1.18	24.83	1.9	17.96	2.0	14.01	2.3	17.05	2.1
Nb	0.49	8.3	0.45	5.55	0.64	6.8	3.62	3.4	5.17	2.8	0.10	19.2
La	245.10	0.7	909.25	0.59	235.77	0.7	865.20	0.7	2208.21	0.7	2130.65	0.8
Ce	557.90	0.8	2004.82	0.53	565.80	0.7	2116.04	0.8	5322.73	0.8	4289.79	0.9
Pr	64.50	0.8	212.44	0.57	66.75	0.8	235.24	0.7	584.26	0.6	454.40	0.8
Nd	242.05	1.1	764.96	0.55	252.25	1.0	859.23	0.8	2031.15	0.9	1621.42	0.8
Sm	41.42	2.1	122.50	0.85	44.82	1.8	131.86	1.3	254.82	1.2	210.71	1.3
Eu	6.97	2.5	18.70	0.99	7.07	2.1	14.02	1.7	29.02	1.4	29.91	1.4
Gd	32.64	2.3	90.32	0.88	33.96	1.9	87.77	1.5	152.70	1.4	130.33	1.6
Tb	4.18	2.4	11.24	0.94	4.45	2.1	10.49	1.6	16.49	1.5	13.07	1.6
Dy	23.21	2.3	63.03	0.86	25.42	1.8	57.34	1.5	86.09	1.4	65.26	1.6
Ho	4.39	2.5	11.53	0.93	4.84	1.9	10.03	1.7	15.14	1.6	11.02	1.7
Er	11.77	2.8	29.67	1.04	12.44	2.2	26.88	1.8	38.60	1.6	26.71	2.2
Tm	1.58	4.0	3.98	1.44	1.57	3.0	3.54	2.8	4.82	2.5	3.23	2.7
Yb	8.84	3.4	23.26	1.29	9.37	2.6	20.28	2.3	26.60	2.2	18.02	2.6
Lu	1.18	4.1	2.95	1.75	1.19	4.0	2.55	3.3	3.18	3.0	2.42	3.3
Pb	104.59	4.2	107.37	2.2	113.67	4.1	56.09	6.9	122.84	6.0	17.28	12.9
Th	793.41	1.0	869.59	0.56	848.69	1.1	2059.56	0.8	5180.41	1.0	666.93	1.0
U	68.46	1.0	67.70	0.64	56.98	1.2	132.13	1.0	144.47	0.8	25.39	1.5
Element	OL2		OL3		OL4		GR40		NUAN		SLAP	
	Wtd Mean	2s (%) (n = 4)	Wtd Mean	2s (%) (n = 6)	Wtd Mean	2s (%) (n = 4)	Wtd Mean	2s (%) (n = 10)	Wtd Mean	2s (%) (n = 26)	Wtd Mean	2s (%) (n = 10)
Li	0.74	8.4	0.85	6.2	0.29	15.6	0.32	20.9	1.30	3.82	0.32	8.6
Si	5443.69	2.9	5601.07	1.7	1828.95	5.8	4617.74	0.8	522.61	1.75	5601.95	2.1
P	225416	1.4	248090	0.8	245386	1.4	205552	0.6	222900	0.35	219760	0.8
Fe	221.91	2.4	242.24	1.6	184.67	2.8	68.73	4.1	286.89	1.08	192.39	1.3
Sr	1612.19	0.9	1628.73	0.6	3600.99	0.9	1781.83	0.5	280.95	0.32	1932.28	0.5
Y	962.86	1.2	1004.81	0.8	353.48	1.1	271.23	0.5	241.90	0.33	290.97	0.8
Zr	0.99	10.5	1.09	6.4	0.93	10.0	8.33	1.8	0.11	9.11	15.20	1.7
Nb	0.19	18.3	0.20	10.5	0.37	13.0	0.09	12.5	Below LOD		0.08	14.8
La	2559.40	0.9	2739.60	0.5	1287.54	1.0	2009.63	0.5	199.57	0.31	2029.70	0.5
Ce	6683.67	1.0	7183.94	0.7	2945.07	1.5	4094.73	0.5	508.58	0.30	4019.35	0.6
Pr	818.38	0.9	872.02	0.5	340.10	0.9	412.62	0.5	61.58	0.38	426.40	0.5
Nd	3147.44	1.0	3368.59	0.6	1264.73	1.1	1468.44	0.5	266.43	0.41	1518.31	0.7
Sm	439.02	1.4	467.58	0.8	179.75	1.8	190.67	0.7	47.95	0.75	198.32	0.9
Eu	71.67	1.2	75.82	0.8	36.32	1.5	26.51	0.9	10.59	0.78	27.89	1.0
Gd	296.82	1.5	316.27	0.9	118.29	1.6	120.87	0.9	46.52	0.73	121.95	1.1
Tb	33.00	1.3	35.22	1.0	13.51	1.9	11.86	1.0	5.89	0.76	12.39	1.1
Dy	178.24	1.5	187.75	1.0	71.32	1.8	58.08	0.9	36.28	0.66	61.62	1.1
Ho	33.62	1.3	35.97	1.0	12.64	2.3	9.72	1.0	7.74	0.67	10.37	1.3
Er	91.12	1.5	97.11	1.0	33.22	1.9	23.36	1.1	23.48	0.68	25.33	1.3
Tm	11.78	2.4	12.59	1.3	4.23	3.1	2.82	1.6	3.41	0.95	3.05	1.9
Yb	68.31	1.9	72.71	1.2	23.35	3.0	15.96	1.5	24.22	0.79	17.08	1.8
Lu	8.90	2.6	9.39	1.6	2.69	4.0	2.14	2.0	4.69	0.83	2.31	2.3
Pb	37.06	7.0	45.41	4.0	12.56	7.2	14.84	8.5	9.41	2.1	16.96	7.8
Th	508.78	1.2	601.24	0.7	67.61	1.4	649.86	0.6	9.33	0.69	653.29	0.7
U	78.39	1.3	88.80	0.8	10.25	2.3	23.88	0.8	28.55	0.46	25.33	0.9

All measurements values are $\mu\text{g g}^{-1}$

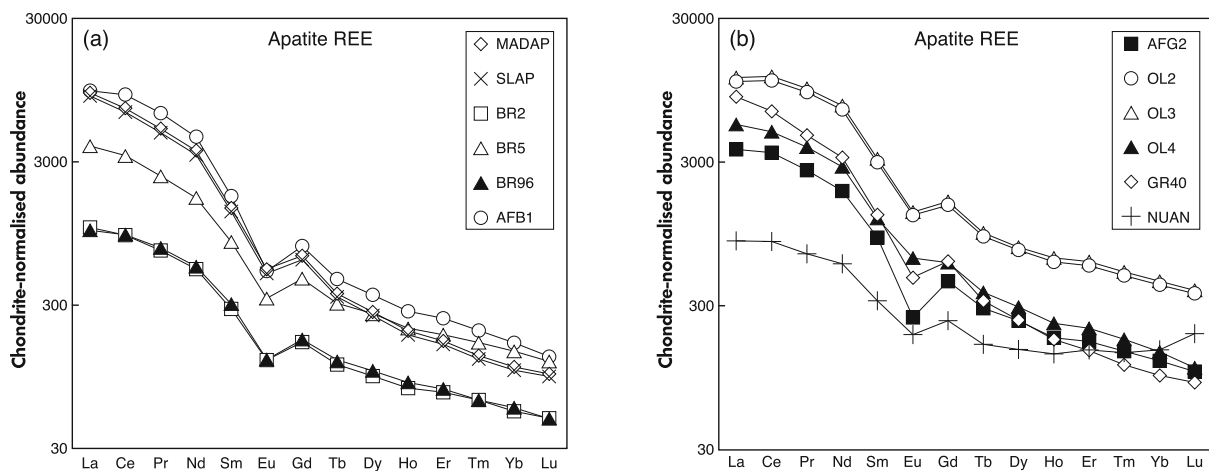


Figure 4. Chondrite-normalised weighted mean REE element patterns for the apatite. Chondritic values are from Anders and Grevesse (1989). The insets show the symbols for each apatite. Uncertainties are typically smaller in size than the symbols.

common Pb composition, Pb loss at different points in time, any variation in the initial time of system closure, or any resetting close to the initial closure of the U-Pb system. For example, the best-fit chord to the uncorrected OL2 data in Figure 5 has an MSWD of 32 when projected onto a Tera-Wasserburg Concordia diagram, and this indicates that there is variability in the isotopic Pb composition, beyond analytical uncertainties, amongst the analysed chips of OL2. The linear regression intercept with the Concordia curve gives an age of 868.75 ± 1.46 Ma. For OL2 the Concordia constrained 3D regressions of the ID-TIMS data gives an unusual common Pb composition, with a $^{206}\text{Pb}/^{204}\text{Pb}$ ratio of 49.09 ± 0.84 , and a $^{207}\text{Pb}/^{204}\text{Pb}$ ratio of 18.54 ± 0.08 . The MSWD of each of the projections of the 3D the regressions used to obtain common Pb compositions onto a Tera-Wasserburg Concordia diagram range from 19 in AFG2 to 270 in AFB1, and this indicate that the different chips of each of the apatite samples analysed by ID-TIMS are not perfectly consistent with the assumption of a single common Pb composition or concordance. Concordia constrained 3D regressions of the ID-TIMS data can be used to obtain the common Pb composition if an apatite is assumed to be concordant and contain a single common Pb component. The analyses from both the BSU and UNIGE laboratories are very consistent and have been pooled and a Concordia constrained 3D linear regression of the uncorrected data used to derive the common Pb composition (Ludwig 2009), which is then used to calculate radiogenic ages for each analysis. The reproducibility issues for high precision U-Pb ID TIMS are well documented, and have been covered in detail in Schaltegger *et al.* (2021).

None of the uncorrected ID-TIMS Pb-Pb apatite data sets produce a true isochron as the MSWD values are all > 2.0 and there must be minor variation of the isotopic composition of Pb in the different analysed chips of apatite, that indicates minor disturbance to the U-Pb system. The ID-TIMS Pb-Pb data for the apatite samples are shown in Figure 6a–e, and the respective calculated York regression ages and 2s uncertainties are: BR2 2052.82 ± 0.63 Ma (MSWD = 140, $n = 8$), BR5 2040.22 ± 0.56 Ma (MSWD = 43, $n = 7$), AFG2 472.77 ± 4.66 Ma (MSWD = 4.6, $n = 10$), AFB1 475.31 ± 5.52 Ma (MSWD = 4.1, $n = 8$), OL2 857.94 ± 3.64 Ma (MSWD of 8.5, $n = 10$). The smaller regression MSWD for the younger apatite samples AFB1 and AFG2 is a reflection of the much larger uncertainties on the measured $^{207}\text{Pb}/^{206}\text{Pb}$ ratios, as can be seen in Figure 7 and Table 3. The Pb-Pb York regression intercepts (Figure 6) are an independent constraint on the initial Pb isotope ratios, which act as a confirmation of the 3D results for common Pb composition.

The weighted mean ages calculated from the ID-TIMS individual analysis data in Figure 7 are within uncertainties identical to the York regression ages for BR2, BR5, AFG2 and AFB1. However, the MSWD of equivalence of the BR2 ages is 19.6, which indicates scatter well outside analytical uncertainties. For BR5 this MSWD equals 6.0, and this results from a single chip that is ~ 2 Ma younger than the others. For AFG2 the MSWD of equivalence is 1.4 and this shows that all of the analysed chips of AFG2 have very consistent $^{207}\text{Pb}/^{206}\text{Pb}$, $^{207}\text{Pb}/^{235}\text{U}$ and $^{206}\text{Pb}/^{238}\text{U}$ ages. For AFB1 the $^{207}\text{Pb}/^{206}\text{Pb}$ age is consistently higher than the $^{207}\text{Pb}/^{235}\text{U}$ and $^{206}\text{Pb}/^{238}\text{U}$ ages and this results in a

Table 3.
U-Pb isotope ratio measurement results for apatite reference samples by ID-TIMS

Sample	Compositional parameters					Radiogenic isotope ratios							207Pb/ 206Pb (g)	±		
	Th/U (b)	206Pb* x10 ⁻¹³ mol (c)	mol % 206Pb* (c)	Pb*/ Pb _c (c)	Pb _c (pg) (c)	206Pb/ 204Pb (d)	208Pb/ 206Pb (e)	207Pb/ 206Pb (e)	% err (f)	207Pb/ 235U (e)	% err (f)	206Pb/ 238U (e)			% err (f)	corr. coef. (f)
BR2																
α1(B)	13.429	58.1156	95.50%	53	113.51	380	3.855	0.126981	0.119	6.579543	0.078	0.375799	0.097	0.090	2056.59	2.09
α2(B)	12.220	31.3973	96.79%	70	43.44	534	3.510	0.126664	0.085	6.542781	0.061	0.374636	0.070	0.173	2052.17	1.49
α3(B)	12.312	25.1462	95.42%	48	50.32	374	3.534	0.126449	0.121	6.530573	0.081	0.374573	0.098	0.089	2049.17	2.14
α4(B)	12.368	20.0524	96.93%	73	26.69	558	3.552	0.126819	0.081	6.556672	0.057	0.374970	0.066	0.149	2054.34	1.42
α5(B)	9.956	25.73151	98.24%	112	190.68	973	2.858	0.126804	0.057	6.560723	0.073	0.375247	0.061	0.660	2054.13	1.00
α1(G)	11.291	47.0949	97.10%	73	58.50	591	3.244	0.127160	0.112	6.586916	0.111	0.375689	0.067	0.294	2059.08	1.97
α2(G)	12.352	57.2923	96.72%	69	80.67	522	3.546	0.126872	0.085	6.566500	0.057	0.375377	0.070	0.104	2055.07	1.51
α3(G)	11.060	32.3559	96.92%	67	42.95	556	3.175	0.126828	0.082	6.562911	0.059	0.375301	0.066	0.147	2054.46	1.45
BR5																
α1(B)	12.712	119.4006	97.02%	83	143.55	674	3.654	0.125716	0.085	6.442967	0.086	0.371701	0.080	0.472	2038.91	1.51
α2(B)	13.655	76.5578	97.85%	121	66.12	935	3.926	0.125852	0.055	6.455162	0.046	0.372001	0.051	0.343	2040.82	0.98
α3(B)	12.465	80.1159	96.40%	67	117.20	558	3.579	0.125704	0.100	6.455586	0.087	0.372466	0.086	0.335	2038.73	1.77
α4(B)	12.973	64.4503	97.24%	90	71.77	729	3.729	0.125943	0.069	6.466616	0.047	0.372393	0.060	0.176	2042.10	1.22
α1(G)	11.806	19.3946	97.89%	108	16.86	948	3.392	0.125840	0.064	6.460423	0.061	0.372342	0.048	0.317	2040.64	1.14
α2(G)	13.214	14.2753	96.96%	81	17.96	661	3.795	0.125787	0.091	6.459845	0.079	0.372465	0.068	0.252	2039.90	1.60
α3(G)	12.902	57.2795	99.06%	264	21.79	2128	3.707	0.125843	0.029	6.459902	0.037	0.372302	0.029	0.634	2040.69	0.52
AFB1																
α1(B)	35.376	14.7144	94.51%	112	33.26	358	11.094	0.056745	0.210	0.594566	0.181	0.075993	0.117	0.049	481.62	4.65
α2(B)	35.192	10.1042	94.18%	104	24.43	338	11.024	0.056625	0.231	0.591408	0.203	0.075749	0.123	0.061	476.95	5.12
α3(B)	35.190	13.3636	94.38%	108	31.00	350	11.020	0.056681	0.213	0.595771	0.181	0.076233	0.119	0.037	479.14	4.71
α4(B)	35.176	7.8348	94.54%	110	17.85	360	11.021	0.056701	0.212	0.595303	0.184	0.076146	0.114	0.051	479.93	4.69
α5(B)	35.501	7.7557	92.07%	75	26.07	248	11.120	0.056666	0.317	0.594074	0.273	0.076036	0.171	0.037	478.54	7.00
α1(G)	35.190	12.3921	93.07%	87	35.80	284	11.046	0.056836	0.312	0.596743	0.285	0.076149	0.149	0.076	485.16	6.89
α2(G)	35.313	10.8879	93.11%	87	31.35	286	11.055	0.056655	0.309	0.595172	0.282	0.076191	0.148	0.070	478.13	6.83
α3(G)	35.066	15.4938	94.51%	111	34.97	358	10.998	0.056828	0.286	0.598739	0.276	0.076415	0.118	0.130	484.85	6.32
AFG2																
α1(B)	15.990	26.9009	91.66%	39	87.38	289	5.006	0.056715	0.287	0.602760	0.226	0.077081	0.183	0.023	480.46	6.4
α2(B)	15.594	13.8027	93.23%	47	36.10	355	4.886	0.056765	0.237	0.603140	0.196	0.077062	0.146	0.057	482.40	5.2
α3(B)	16.000	15.0551	91.19%	36	52.13	273	5.014	0.056791	0.306	0.603703	0.243	0.077098	0.193	0.030	483.42	6.8
α4(B)	15.803	18.0937	93.20%	48	47.37	354	4.947	0.056687	0.237	0.601734	0.193	0.076988	0.147	0.047	479.36	5.2
α5(B)	15.874	8.0517	92.22%	41	24.67	308	4.971	0.056737	0.272	0.602878	0.224	0.077065	0.168	0.061	481.34	6.0
α1(G)	16.031	5.6968	88.41%	27	27.04	207	5.018	0.056686	0.457	0.601767	0.395	0.076992	0.262	0.077	479.35	10.1
α2(G)	15.409	10.5246	92.34%	41	31.54	313	4.824	0.056705	0.302	0.602769	0.267	0.077095	0.167	0.088	480.09	6.7

**Table 3 (continued).
U-Pb isotope ratio measurement results for apatite reference samples by ID-TIMS**

Isotopic ages				Sample (radiogenic + initial Pb) isotope ratios										U	Pb		
²⁰⁷ Pb/ ²³⁵ U (g)	± (f)	²⁰⁶ Pb/ ²³⁸ U (g)	± (f)	²³⁸ U/ ²⁰⁶ Pb (h)	% err (f)	²⁰⁷ Pb/ ²⁰⁶ Pb (h)	% err (f)	²⁰⁴ Pb/ ²⁰⁶ Pb (h)	% err (f)	corr. coef. 8/6-7/6	corr. coef. 8/6-4/6	corr. coef. 7/6-4/6	Mass (mg)	(i)	(j)	(i)	(j)
2040.45	0.69	2040.99	1.20	2.605079	0.050006	0.146873	0.198390	0.001470	1.501341	-0.829845	-0.813789	0.984455	0.010	92	147.6		
2040.46	0.33	2040.22	0.51	2.660829	0.024598	0.132408	0.059401	0.000459	1.279757	-0.474488	-0.405524	0.921473	0.010	369	576.7		
473.78	0.68	472.16	0.53	12.415911	0.044692	0.097031	0.302891	0.002752	0.738505	-0.873903	-0.863087	0.990725	0.010	463	374.9		
471.77	0.77	470.70	0.56	12.416984	0.060873	0.099127	0.428847	0.002902	1.013491	-0.931084	-0.920802	0.991773	0.010	319	256.1		
474.55	0.69	473.60	0.54	12.361168	0.046755	0.097887	0.329700	0.002814	0.790880	-0.917814	-0.910572	0.993974	0.010	419	338.5		
474.25	0.70	473.08	0.52	12.403952	0.075653	0.096264	0.574018	0.002703	1.408291	-0.968714	-0.965193	0.996617	0.010	246	198.4		
473.47	1.08	472.42	0.78	12.097599	0.075053	0.114647	0.462696	0.003956	0.925752	-0.961109	-0.954480	0.994153	0.010	244	198.8		
475.16	1.03	473.10	0.68	12.204586	0.049983	0.107711	0.314575	0.003473	0.694400	-0.913166	-0.877492	0.962963	0.010	389	315.2		
474.17	1.07	473.35	0.68	12.204171	0.054821	0.107188	0.360012	0.003448	0.788746	-0.947326	-0.921325	0.973337	0.010	342	277.2		
476.43	1.05	474.69	0.54	12.347807	0.043728	0.097118	0.287685	0.002752	0.743442	-0.853394	-0.785460	0.932760	0.010	485	391.6		
478.98	0.86	478.68	0.84	11.884862	0.029027	0.108167	0.142615	0.003444	0.309320	-0.719153	-0.694969	0.982485	0.010	836	347.4		
479.22	0.75	478.56	0.67	12.097199	0.046617	0.098208	0.314643	0.002775	0.768895	-0.880701	-0.870697	0.990493	0.010	429	173.9		
479.58	0.93	478.78	0.89	11.825516	0.042196	0.110945	0.245233	0.003625	0.519730	-0.873526	-0.860910	0.990242	0.010	468	195.0		
478.33	0.74	478.12	0.68	12.102257	0.037746	0.098440	0.239555	0.002796	0.584778	-0.828421	-0.815521	0.984139	0.010	563	230.3		
479.06	0.86	478.58	0.78	11.971303	0.071684	0.104154	0.498284	0.003175	1.127477	-0.970286	-0.966470	0.996329	0.010	250	103.2		
478.35	1.51	478.15	1.21	11.494129	0.097737	0.127457	0.535158	0.004736	1.001007	-0.965001	-0.953009	0.988080	0.010	177	74.6		
478.99	1.02	478.76	0.77	11.979066	0.057006	0.103566	0.384210	0.003137	0.889146	-0.936303	-0.913433	0.979256	0.010	327	131.6		
480.41	1.15	478.67	1.00	11.708321	0.028815	0.116842	0.116381	0.004011	0.261490	-0.654039	-0.550206	0.876697	0.010	924	376.6		
477.95	1.24	477.70	0.95	11.785180	0.060637	0.114101	0.371811	0.003844	0.776878	-0.950887	-0.927285	0.976593	0.010	297	122.7		
868.45	0.66	868.68	1.48	6.359207	0.024484	0.093532	0.063372	0.001681	0.246385	-0.357741	-0.288111	0.964467	0.010	1195	490.1		
868.27	0.81	867.61	1.84	6.240775	0.029070	0.099253	0.068577	0.002053	0.231207	-0.350546	-0.272957	0.955372	0.010	1018	427.5		
869.45	0.75	869.22	1.62	6.308332	0.031796	0.095683	0.086161	0.001818	0.310028	-0.372087	-0.300321	0.944106	0.010	868	359.8		
867.76	0.69	867.76	1.53	6.349953	0.027080	0.094259	0.111256	0.001729	0.422424	-0.523166	-0.490898	0.977548	0.010	673	276.3		
870.06	1.09	869.71	1.77	6.278831	0.063947	0.096859	0.047376	0.001893	0.125311	-0.366011	-0.185992	0.9274731	0.010	2239	934.8		
869.73	1.15	869.21	1.85	6.259541	0.053500	0.097547	0.313209	0.001943	1.109509	-0.761225	-0.744057	0.984199	0.010	225	94.6		
869.70	0.90	870.02	1.64	6.309349	0.033861	0.095662	0.118883	0.001815	0.452155	-0.465508	-0.396183	0.926947	0.010	620	256.9		
868.77	1.61	868.29	2.25	6.194916	0.079201	0.101050	0.525696	0.002172	1.715100	-0.894024	-0.884051	0.989609	0.010	127	54.3		

Table 3 (continued).
U-Pb isotope ratio measurement results for apatite reference samples by ID-TIMS

Isotopic ages				Sample (radiogenic + initial Pb) isotope ratios							U	Pb				
$^{207}\text{Pb}/^{235}\text{U}$ (g)	± (f)	$^{206}\text{Pb}/^{238}\text{U}$ (g)	± (f)	$^{238}\text{U}/^{206}\text{Pb}$ (h)	% err (f)	$^{207}\text{Pb}/^{206}\text{Pb}$ (h)	% err (f)	$^{204}\text{Pb}/^{206}\text{Pb}$ (h)	% err (f)	corr. coef. 8/6-7/6	corr. coef. 8/6-4/6	corr. coef. 7/6-4/6	Mass (mg)	(i)	(i)	(i)
870.26	0.69	869.88	1.60	6.305836	0.019938	0.095599	0.046404	0.001810	0.180315	-0.316017	-0.257914	0.918317	0.010	1580	657.3	
868.05	0.66	867.69	1.56	6.335092	0.019636	0.094986	0.036540	0.001774	0.144502	-0.254953	-0.203915	0.919344	0.010	2024	838.3	

(a) a1, a2, etc. are labels for individual apatite fragments. (b) denotes Boise State University analysis. (c) denotes University of Geneva analysis

(b) Model Th/U ratio calculated from radiogenic $^{206}\text{Pb}/^{206}\text{Pb}$ ratio and $^{207}\text{Pb}/^{235}\text{U}$ age.

(c) Pb* and Pbc represent radiogenic and common Pb, respectively; mol % $^{206}\text{Pb}^*$ with respect to radiogenic, blank and initial common Pb.

(d) Measured ratio corrected for spike and fractionation only. Fractionation was monitored and corrected by the double spikes of the ET2535 tracer.

(e) Corrected for fractionation, spike, and common Pb; up to 1 pg of common Pb was assumed to be procedural blank. $^{206}\text{Pb}/^{204}\text{Pb} = 18.35 \pm 1.5\%$; $^{207}\text{Pb}/^{204}\text{Pb} = 15.60 \pm 0.5\%$; $^{208}\text{Pb}/^{204}\text{Pb} = 38.08 \pm 1.0\%$ (all uncertainties 1 σ). Excess over blank was assigned to initial common Pb with a composition estimated from a 3-D "Total Pb" isochron regression, with arbitrary uncertainties of 1% ($^{206}\text{Pb}/^{204}\text{Pb}$) and 0.5% ($^{207}\text{Pb}/^{204}\text{Pb}$).

(f) Errors are 2-sigma, propagated using the algorithms of Schmitz and Schoene (2007). U and Th mass fractions are approximate as they are based on an assumed mass for the sample.

(g) Calculations are based on the decay constants of Jaffey *et al.* (1971). $^{206}\text{Pb}/^{238}\text{U}$ and $^{207}\text{Pb}/^{235}\text{U}$ ages corrected for initial disequilibrium in $^{230}\text{Th}/^{238}\text{U}$ using Th/U (integral) = 3.

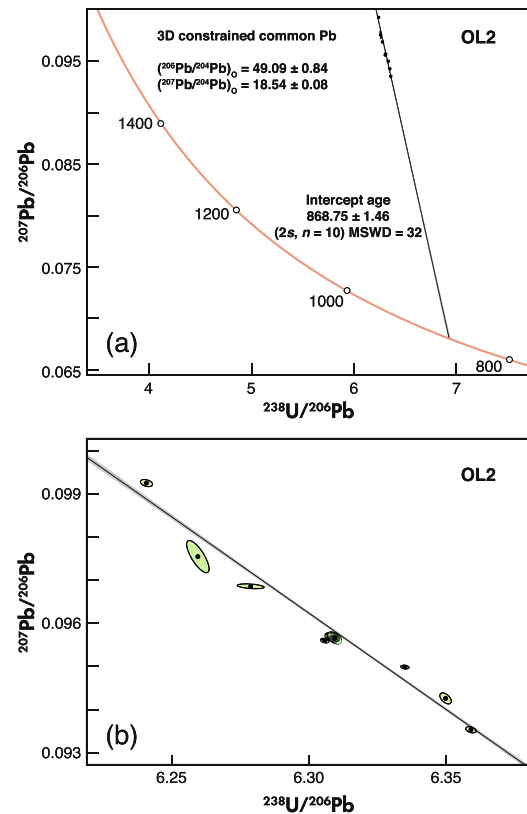


Figure 5. (a) Uncorrected ID-TIMS U-Pb data for OL2 plotted on a Tera-Wasserburg Concordia diagram, along with the Concordia intercept age obtained from linear regression through the points, and the 3D Concordia constrained common Pb composition for OL2. (b) An expanded view of the OL2 data showing the scatter about the Type 1 Discordia fit (Vermeesch 2018).

MSWD of 12.4. For OL2 the weighted mean value from Figure 6 is not within uncertainties of the York regression age value. Even so, OL2 has a low MSWD of 2.2. This reflects the large uncertainties on the corrected ages due to the unusual Concordia constrained common Pb composition of OL2, which has high values for the $^{206}\text{Pb}/^{204}\text{Pb}$ and $^{207}\text{Pb}/^{204}\text{Pb}$ ratios (Table 4).

The common Pb corrected data for the ID-TIMS analyses of BR2, BR5, AFG2 and AFB1 are plotted in Wetherill Concordia diagrams in Figure 8a-d. The MSWD of equivalence for the common Pb corrected data (Table 4) is a measure of the isotopic homogeneity of the individual apatite. BR2 and AFB1, with respective values of 25 and 13 are the least homogeneous apatite, and Figure 8 shows that the data for BR2, BR5 and AFB1 spread along the Concordia, beyond analytical uncertainties. The spread of

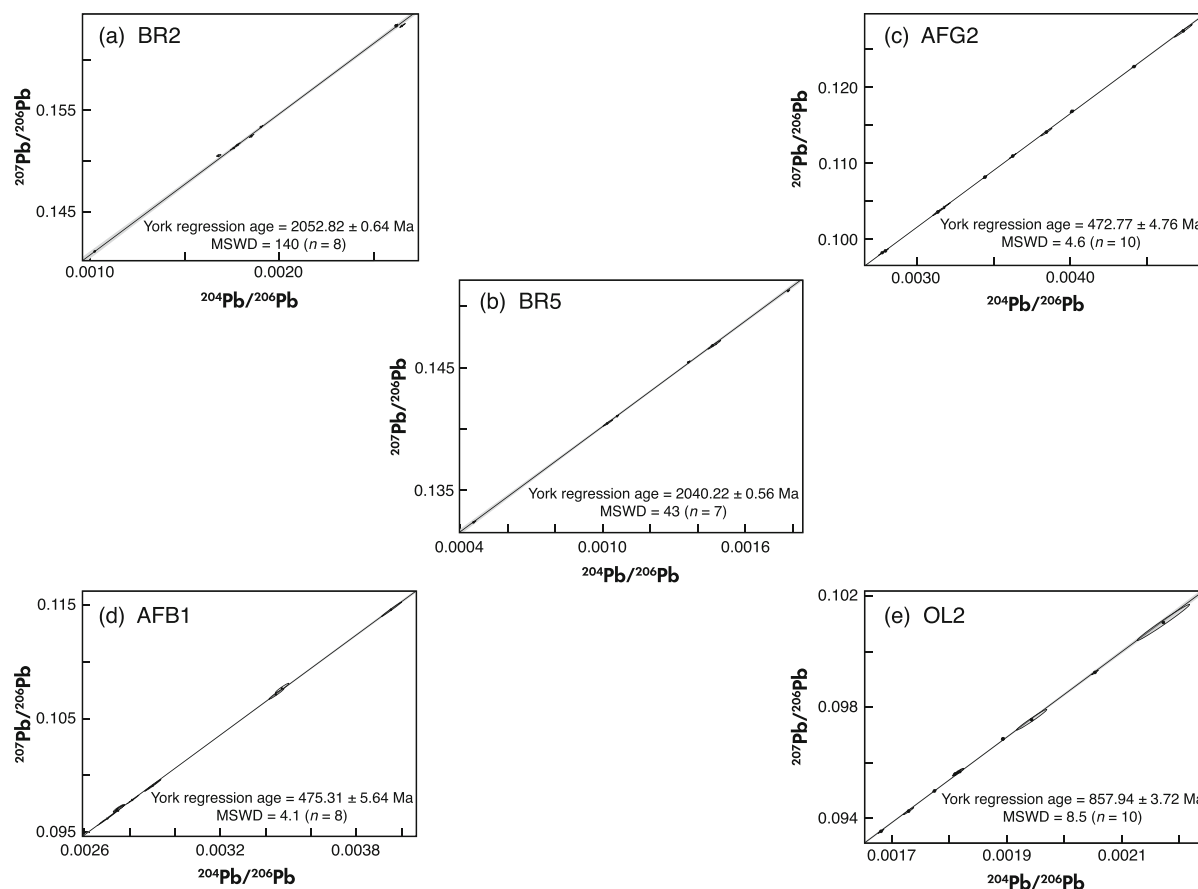


Figure 6. ID-TIMS Pb-Pb isochron diagrams for the BR2, BR5, AFG2, AFB1 and OL2 apatite. The MSWD of fit for the York linear regression of the data and the calculated isochron age are given. Uncertainties are 2s. Larger individual diagrams are given in the online supporting information (Figure S6).

BR2 along the Concordia, where essentially all points are concordant is suggestive of isotopic resetting within a few million years of apatite formation. BR5 is the next-most homogeneous apatite, with a MSWD of equivalence of 6.6, with all but one chip plotting as a group at 2040 Ma. The apatite with the best isotopic homogeneity is AFG2, and this is the only apatite for which the calculation of a Concordia age for the common Pb corrected data is justified by the MSWD of equivalence, which is 1.1. The Concordia ages for apatites BR2, BR5, AFG2 and AFB1 (Figure 8) are the best quantitative estimate of the age of the apatite samples, assuming concordance and equivalence.

The ID-TIMS data show that accurate U-Pb ages can only be obtained when the actual common Pb composition is known. This has previously been discussed in detail by Krestianinov *et al.* (2021) who completed an ID-TIMS study of U-rich apatite from the Adirondacks, and we return to this issue in the discussion of results segment. The apatite ID-TIMS data sets from Geneva and Boise demonstrate the excellent

reproducibility of TIMS measurements between two laboratories using the same calibration for the EARTHTIME U-Pb spikes.

SHRIMP U-Pb

The summarised SIMS results (Table 4) are from mounts containing multiple chips of the apatite samples and they give some indication of 3-dimensional homogeneity. The common Pb corrected results from individual spot analyses of the apatite are plotted on Wetherill Concordia diagrams in Figure 9, along with an uncertainty ellipse for the Concordia age from all the SHRIMP analyses of each apatite, and the MSWD for concordance and equivalence. Uncertainties in the figures and Table S1 are one standard deviation for individual analyses and 2 standard error on the Concordia age. Only BR5 has a MSWD of concordance that truly justifies the assumption of concordance. The SIMS Concordia age for BR2, AFG2 and AFB1 is given, as it allows comparison with the ID-TIMS Concordia age.

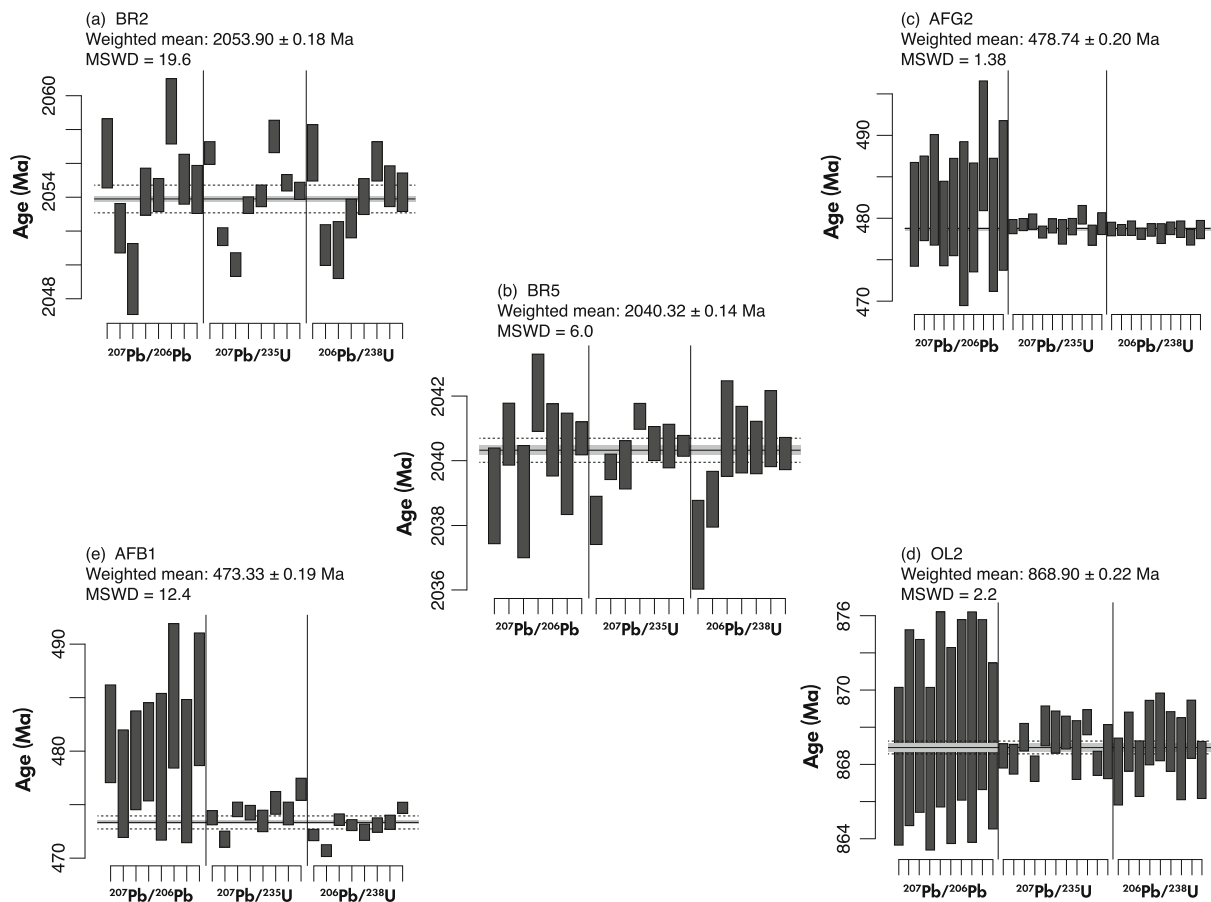


Figure 7. ID-TIMS U-Pb dates from the University of Geneva data and Boise State University. The Concordia constrained 3D $^{207}\text{Pb}/^{204}\text{Pb}$, $^{207}\text{Pb}/^{235}\text{U}$ and $^{206}\text{Pb}/^{238}\text{U}$ ages are shown for the BR2, BR5, AFG2, AFB1 and OL2 apatite. Individual range bars represent $2s$ uncertainties. All data were corrected using the common Pb composition for each apatite given in Table 4. Weighted mean ages include all age data for each apatite and the MSWD is a measure of equivalence of the ages.

The analysed apatite samples were chosen for U-Pb measurement because they have highest U and lowest common Pb of the apatite samples we examined. Even so, they still contain significant common Pb, and this is reflected in the relatively low $^{206}\text{Pb}/^{204}\text{Pb}$. The mean SIMS $^{206}\text{Pb}/^{204}\text{Pb}$ values for BR2, BR5, AFG2, AFB1 and OL2 are respectively, 787, 1031, 358, 395 and 341 (Table 4). In comparison, a zircon U-Pb RM of similar age typically has a $^{206}\text{Pb}/^{204}\text{Pb}$ ratio $> 10,000$ (e.g., Nasdala *et al.* 2008).

The SHRIMP data are sensitive to the common Pb correction because of the relatively large amount of common Pb in most apatite. The percentage of ^{206}Pb that is common Pb varies between $\sim 0.5\%$ and $> 10\%$ in individual SHRIMP spots, and this is comparable to the ID-TIMS measurement of radiogenic ^{206}Pb percentages. The data in Figure 9 have been corrected for common Pb, using the common Pb

compositions derived from the Concordia constrained 3D linear regression intercept of the ID-TIMS data with the common Pb plane (Table 4). None of the 3D derived common Pb compositions are close to the Stacey and Kramers (1975) common Pb growth curve composition at the radiogenic age of the measured apatite (Table 4), and this shows that the common Pb composition of an apatite must be known if accurate SIMS ages are to be obtained. When the Stacey and Kramers (1975) common Pb growth curve composition is used, the SIMS result is shifted far away from the correct age. For example, the SHRIMP OL2 age using the Stacey and Kramers (1975) common Pb growth curve composition for common Pb correction is ~ 70 Ma years too old.

The common Pb corrected SHRIMP data for BR2, BR5, AFG2 and AFB1 have respective MSWD of equivalence values of 1.4, 1.1, 2.1 and 1.6, indicating they are close to

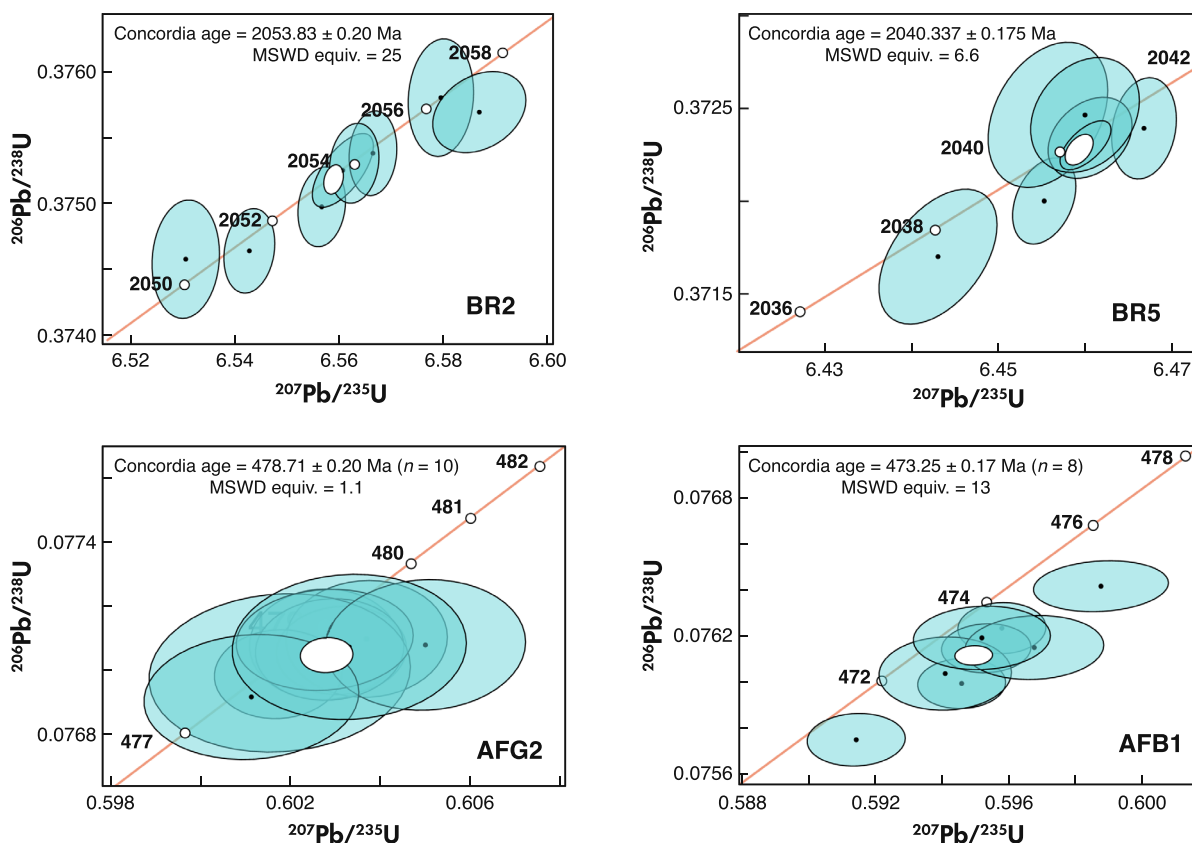


Figure 8. Wetherill Concordia diagrams showing the ID-TIMS data corrected for common Pb derived from the Concordia constrained 3D regression for each apatite. The Concordia age is a weighted, objective, quantitative measure of the age of the apatite if it is concordant. Uncertainties and ellipses are $2s$, and the MSWD is a measure of equivalence of the data points.

Table 4.
Apatite ID-TIMS and SHRIMP ages and common Pb compositions

Apatite	ID-TIMS age	<i>n</i>	MSWD (C)	MSWD (EC)	SHRIMP age	<i>n</i>	MSWD (C)	MSWD (EC)	$^{206}\text{Pb}/^{204}\text{Pb}$	Pbc 3D 6/4	Pbc 3D 7/4	Pbc S-K 6/4	Pbc S-K 7/4
BR2	2053.83 ± 0.21	8	0.37	24	2055.5 ± 5.4	101	16	1.4	787	17.25	16.12	15.05	15.16
BR5	2040.34 ± 0.09	7	3	6.3	2044.7 ± 6.3	126	2.5	1.1	1031	20.29	16.90	15.08	15.17
AFG2	478.71 ± 0.22	10	7.6	1.4	477.1 ± 1.5	140	96	2.1	358	24.10	16.32	17.95	15.58
AFB1	473.25 ± 0.09	8	41	15	474.1 ± 1.7	144	59	1.6	395	19.72	15.80	17.96	15.59
OL2	868.87 ± 0.25	10	0.3	3.0	866.9 ± 5.5	103	0.017	1.1	341	49.09	18.54	17.3	15.53

ID-TIMS age is the weighted mean 3D concordia intercept age.

SHRIMP Age is the weighted mean age from individual analyses and are taken from Figure 9.

MSWD(C) of concordance and the MSWD(EC) of equivalence and concordance are defined in Ludwig (2003).

$^{206}\text{Pb}/^{204}\text{Pb}$ is the mean value from SHRIMP analyses

For the ID-TIMS data the MSWD(C) and MSWD(CE) are for the 3D concordia intercept ages from the individual analyses.

Reference materials for the individual SIMS data sets are given in the online supporting information data table.

For the SHRIMP data the MSWD(C) and MSWD(CE) are from individual analyses ages corrected using the ID-TIMS 3D intercept derived common Pb composition.

Pbc 3D is the common Pb ratio derived from the ID-TIMS (3D) concordia constrained regression.

Pbc S-K is the common Pb ratio from the Stacey and Kramer (1975) single stage growth curve at the SHRIMP age.

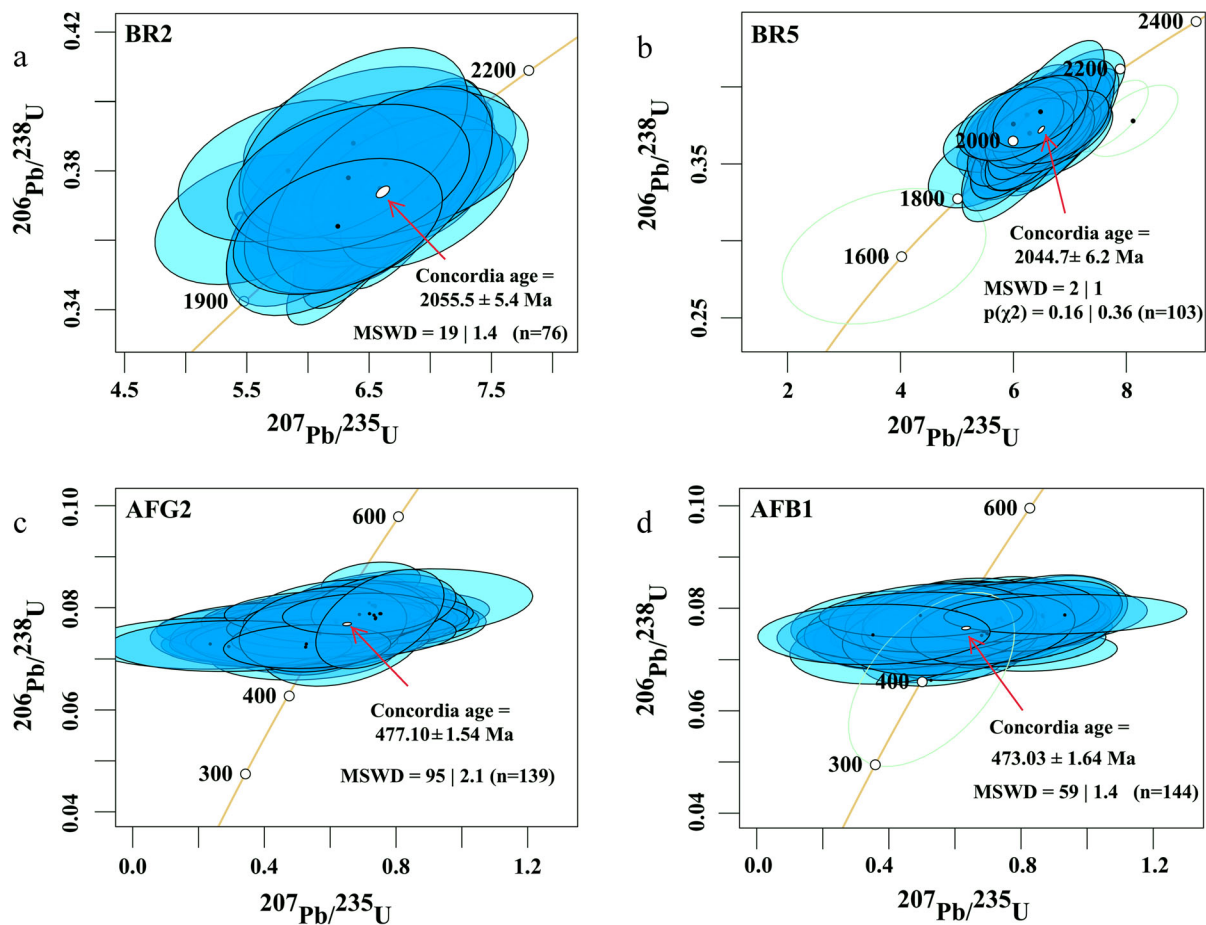


Figure 9. Wetherill Concordia diagrams showing the common Pb corrected SIMS U-Pb data for the BR2, BR5, AFG2, and AFB1 apatite. Individual ellipses are 1s uncertainties. The central white ellipse within the data cloud, identified with a red arrow, is the Concordia age and 2s. All data is corrected using the Concordia constrained 3D regression common Pb composition derived from the ID-TIMS data for each apatite. The AFB1 is corrected for common Pb using the ^{207}Pb correction method for the SIMS data.

homogeneous ($\text{MSWD} = 1$) at the sampling volume and measurement uncertainty of the ion microprobe, when corrected for common Pb (Figure 9a–d). The calculated SHRIMP Concordia age for BR2, BR5, AFG2 and AFB1 are identical, within uncertainties, to the ID-TIMS Concordia ages (Table 4) when the ID-TIMS derived common Pb composition is used for common Pb correction. The MSWD of concordance for the SHRIMP data ranges between 2.5 in BR5 to 96 in AFG2. Taken at face value, this suggests that the SIMS data indicate the apatite are not concordant. However, the SIMS data is highly sensitive to statistical fluctuations of the background and ^{204}Pb measurements, or $^{207}\text{Pb}/^{206}\text{Pb}$ ratio in young samples, and this can result in over or under correction for common Pb, and a spread of data points about the Concordia. Overall, the individual SIMS analysis data for BR2, BR5, AFG2 and AFB1 show that each apatite has good reproducibility at the SHRIMP

level of uncertainty, and this suggest that they can be useful as SIMS RM. There is variation of U and Th abundances in different chips of each apatite, but no relationship between U and Th mass fraction and age is apparent in the SHRIMP data. Because we focused on apatite with a restricted range of major element composition, such that they are all fluoroapatite, it is unlikely that there would be a matrix effect on the SIMS data from the major elements. The NBS 610 glass was monitored to ensure there was no fractionation of the $^{207}\text{Pb}/^{206}\text{Pb}$ ratio. Variation in the trace elements (U, Th, Hf etc.) that produce matrix effects in xenotime, monazite and zircon (Cross and Williams 2018 and references therein) are at very low levels in the apatite we studied and there is no identifiable matrix effects. Even AFB1, which has extremely high Th for apatite, only has 0.4% Th. The biggest difference in the U mass fractions between the apatite studied by SIMS is $\sim \mu\text{g g}^{-1}$, and the

Table 5.
Sulfur isotopic composition of apatite reference samples from gas source mass spectrometry and SIMS

Gas source		OL2	OL4	GR40	AFB1	AFB1	SLAP	MADAP	BR96	BR96	AFG2	DUR B*	IAEA-S-1 for IRMS data		
IRMS	$10^3\delta^{33}\text{S}$	4.723	5.671	7.406	6.939	7.045	6.829	6.788	9.368	9.255	8.663	-0.88 ± 0.30	$10^3\delta^{33}\text{S}$	-0.061	
	$10^3\delta^{34}\text{S}$	9.152	11.162	14.694	13.687	13.802	13.386	13.298	19.011	18.722	17.037	-1.39 ± 0.48	$10^3\delta^{34}\text{S}$	-0.3	
	$10^3\delta^{36}\text{S}$	18.13	20.96	28.24	25.60	26.24	25.01	24.73	35.48	35.52	32.03		$10^3\delta^{36}\text{S}$	-1.27	
	$\Delta^{33}\text{S}$	0.020	-0.062	-0.134	-0.087	-0.039	-0.042	-0.039	-0.377	-0.343	-0.074	-0.134	$\Delta^{33}\text{S}$	0.094	
	$\Delta^{36}\text{S}$	0.67	-0.35	0.13	-0.56	-0.14	-0.58	-0.69	-0.95	-0.35	-0.59		$\Delta^{36}\text{S}$	-0.7	
	Wt% S	0.23	0.11	0.29	0.45	0.45	0.28	0.26	0.36	0.36	0.43				
SIMS	Session 1	$10^3\delta^{33}\text{S}$	4.18 ± 0.62	4.26 ± 0.78	6.07 ± 0.72	6.10 ± 0.74		6.83 ± 0.72	6.11 ± 0.64		8.95 ± 0.82	8.12 ± 0.60	-1.35 ± 1.14		
			(1 nA)	$10^3\delta^{34}\text{S}$	8.66 ± 0.56	8.04 ± 1.36	11.29 ± 0.62	12.21 ± 1.0	#(13.34 ± 0.56)	12.23 ± 0.68		17.97 ± 1.26	16.15 ± 0.64	-3.12 ± 0.90	
	Session 2	$10^3\delta^{33}\text{S}$	4.22 ± 0.34	6.31 ± 0.36	6.60 ± 0.42		6.83 ± 0.28	6.67 ± 0.42		9.39 ± 0.44	8.58 ± 0.34	-1.10 ± 0.75			
			(2 nA)	$10^3\delta^{34}\text{S}$	7.77 ± 0.74	12.65 ± 0.48	13.62 ± 0.42		#(13.34 ± 0.34)	13.05 ± 0.30		18.67 ± 0.36	17.35 ± 0.50	-2.62 ± 0.42	
	Session 3	$10^3\delta^{33}\text{S}$	24.83 ± 0.80						Session 4	$10^3\delta^{33}\text{S}$	9.20 ± 0.72	#(17.03 ± 0.50)			
			(2 nA)**	$10^3\delta^{34}\text{S}$	-7.162 ± 0.56					(0.3nA)	$10^3\delta^{34}\text{S}$	17.77 ± 0.80	8.66 ± 0.50		
	Session 5 [^]	$10^3\delta^{33}\text{S}$	4.80 ± 0.40	4.36 ± 0.74	7.08 ± 0.26	7.60 ± 0.30		6.83 ± 0.38	7.04 ± 0.46		9.40 ± 0.36	9.31 ± 0.54	-0.90 ± 0.50		
			(3 nA)	$10^3\delta^{34}\text{S}$	8.75 ± 0.66	7.84 ± 0.52	13.23 ± 0.38	15.00 ± 1.10	#(13.39 ± 0.30)	12.70 ± 0.88		19.72 ± 0.58	18.46 ± 0.42	-3.30 ± 0.92	
		$\Delta^{33}\text{S}$	0.30 ± 0.46	0.33 ± 0.88	0.29 ± 0.32	-0.10 ± 0.56		-0.04 ± 0.44	0.52 ± 0.60		-0.70 ± 0.42	-0.15 ± 0.50	0.80 ± 0.62		
		S $\mu\text{g g}^{-1} \pm 2\text{SE (WDS)}$	2042 ± 200	921 ± 40	2683 ± 160	4484 ± 40	4484 ± 40	3483 ± 80	2763 ± 120	3483 ± 120	3483 ± 120	4925 ± 200	1161 ± 160*		

IRMS

Gas source data is reported relative to the values for IAEA-S-1 on the VCDT scale that are listed in the table.

$\Delta^{33}\text{S}$ values calculated with following expression: $\Delta^{33}\text{S} = \delta^{33}\text{S} - [(\delta^{34}\text{S}/1000 + 1)^{0.515} - 1] * 1000$

$\Delta^{36}\text{S}$ values calculated with following expression: $\Delta^{36}\text{S} = \delta^{36}\text{S} - [(\delta^{34}\text{S}/1000 + 1)^{1.90} - 1] * 1000$

Duplicate analyses were completed for AFB1 and BR96 apatite.

IRMS Wt% S uncertainty is < 10%.

IRMS uncertainties for $10^3\delta^{33}\text{S}$, $10^3\delta^{34}\text{S}$, $10^3\delta^{36}\text{S}$, $\Delta^{33}\text{S}$, $\Delta^{36}\text{S}$ are respectively, 0.1, 0.2, 0.5, 0.5 and 1.0.

SIMS

*Recommended value and 95% CI; (Hammerli *et al.* 2021).

SIMS values are all mean $10^3\delta^{33}\text{S}$ and $10^3\delta^{34}\text{S}$ VCDT. Uncertainties are 2 standard deviation.

Data were collected in sets of ten analyses for each sample. If not, () gives the number of analyses.

[^] Data were collected in sets of ten analyses for each sample, but with seventy measurement cycles in each analysis.

Reference Material (RM) for each session.

Session 4 comprised 100 analyses of BR96 and ten of AFG2.

Session 3 was a homogeneity test and did not use a RM.

**Session 3 data is uncorrected raw data.

ΣREE is ~ 1%. The overall effect of these differences is likely to be < 1% on the U/Pb ratio, and given the large uncertainties on U/Pb data for analysis of a mineral with 50–150 $\mu\text{g g}^{-1}$ U we have not identified a matrix effect in our data. The individual measurement results from SHRIMP are given in Table S1.

Sulfur isotope compositions

The WDS SO_3 mass fraction in the apatites we examined ranges from 1.2% in AFG2 to 0.1% for NUAN.

The low S content of NUAN, prevented SIMS S isotope determination. BR2, BR5 and BR96 are all from the same Brazilian locality and only BR96 was chosen for IRMS S isotope determination. The S content of the eight apatites analysed by laser fluorination IRMS ranges from 921 $\mu\text{g g}^{-1}$ in OL4, to 4925 $\mu\text{g g}^{-1}$ in AFG2. The $10^3\delta^{34}\text{S}$ value ranges from 9.15 ± 0.2 in OL2 to 18.87 ± 0.2 in BR96. The oldest apatite in Table 5, BR96, with an age of ~2050 Ma, is the only apatite analysed for S isotopic composition that shows evidence for MIF S in the IRMS data, with a mean $\Delta^{33}\text{S}$ value of -0.360. The lack of a MIF S in the other apatite samples is expected, as MIF of S isotopes is rare in samples

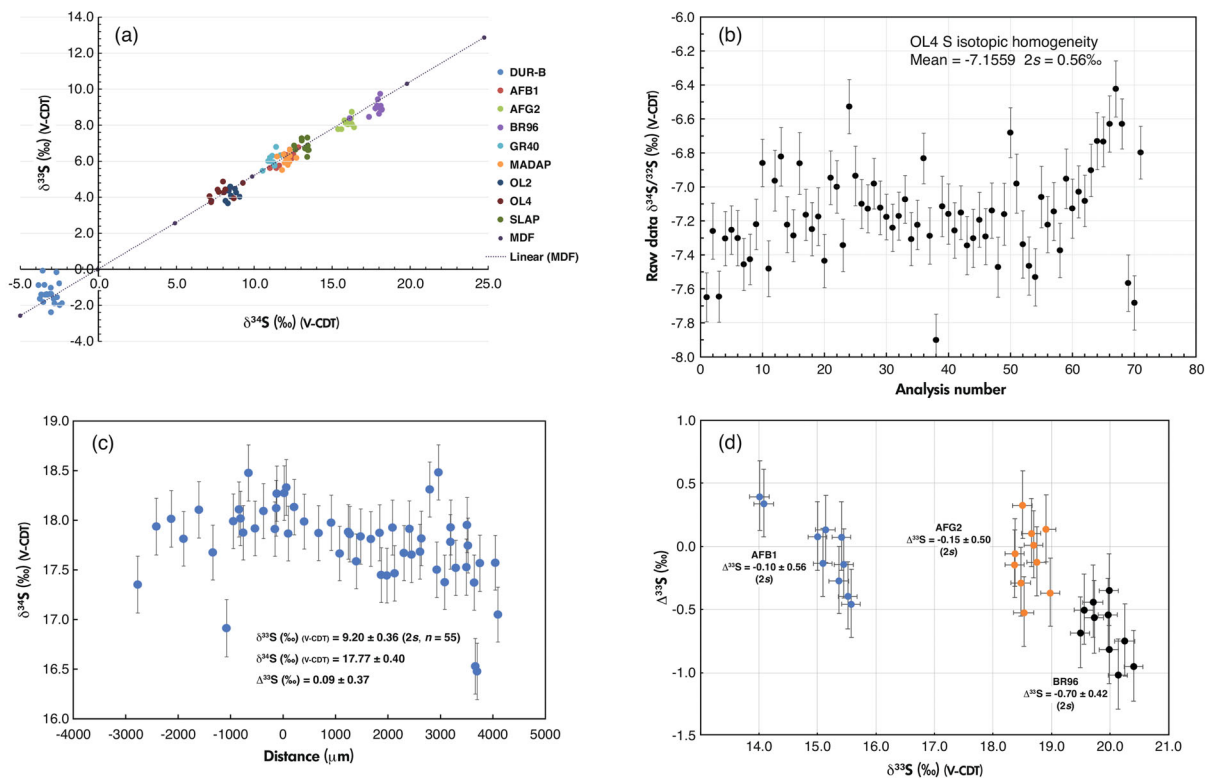


Figure 10. Sulfur isotope data for apatite. (a) $10^3 \delta^{33}\text{S}$ (V-CDT) vs. $10^3 \delta^{34}\text{S}$ (V-CDT) normalised to the IRMS value of the SLAP apatite. Analyses were undertaken on single or multiple large, 500–1000 μm , chips of each apatite. (b) Raw data $10^3 \delta^{33}\text{S}$ (V-CDT) for seventy homogeneity measurements of OL4. Uncertainties are the repeatability precision (“internal error”) at 2s. (c) $10^3 \delta^{34}\text{S}$ (V-CDT) normalised to the IRMS value of sample AFG2 for a 7 mm, cross-sectional, core to rim traverse of a large fragment of BR96. Uncertainties are the combined single analysis “internal” and multiple analysis “external” uncertainties at 2s. (d) Long count interval $10^3 \delta^{33}\text{S}$ (V-CDT) vs. $10^3 \delta^{34}\text{S}$ (V-CDT) for AFB1, AFG2 and BR96 normalised to the IRMS value of sample AFG2. In each session, repeated analyses of a small area within a reference grain of Durango B, OL4, SLAP or AFG2, were used for drift correction and calibration using the IRMS isotopic ratios in Table 5.

that are younger than 2.0 Ga (Farquhar and Wing 2003). The duplicate analyses of AFB1 and of BR96 are within the IRMS uncertainties identical and homogeneous. The measured $\Delta^{33}\text{S}$ values are slightly positive in OL2 and GR40, but negative in all the other apatite samples. Based on the variation in $\Delta^{36}\text{S}$ of the duplicates for AFB1 and BR96 in the IRMS data and the measurement uncertainty we have not been able to identify any MIF of $\Delta^{36}\text{S}$ in any of the apatite.

SIMS S isotope measurements show that most of the analysed apatite have good isotopic homogeneity at the intra-grain level (Table 5, Figure 10a), with the $\delta^{34}\text{S}$ 2s for ten analyses being between 0.28 and 1.36‰, and the $\delta^{33}\text{S}$ 2s being between 0.26 and 0.82‰. As expected, the 2s values are strongly tied to the primary beam intensity

and the mass fraction of S in the apatite. For example, in Session 1 a 1nA primary beam resulted in the $\delta^{33}\text{S}$ 2s being from 0.56 to 0.82‰, while in Session 2, a 2 nA primary beam resulted in the $\delta^{33}\text{S}$ 2s being from 0.34 to 0.44‰. In session 5, where a 3 nA primary beam was used along with seventy cycles AFB1 and MADAP have larger $\delta^{34}\text{S}$ 2s, respectively 1.10 and 0.88‰, suggesting they are more heterogeneous than the other apatite. Two apatite reference samples were studied in greater detail. Seventy analyses on a dozen large, 200 μm , grains of OL4 show that this low S apatite is relatively homogeneous, with the $\delta^{34}\text{S}$ 2s = 0.56‰, and the $\delta^{33}\text{S}$ 2s < 0.80‰, and OL4 will be useful as a low S isotope RM (Figure 10b). A twenty-six-point, cross-sectional core-to-rim analytical traverse of BR96 in Session 4 shows that this 18 g crystal is not homogeneous in S isotopic composition at this length-

Table 6.
Strontium isotope ratios, selected trace element mass fractions and trace element ratios for apatite reference samples

Apatite	$^{87}\text{Sr}/^{86}\text{Sr}$	2s	Sr	Y	Er	Yb	Sr/Y	Sr/Er	Sr/Yb
BR2	0.709955	0.000035	367	123	12.0	8.8	2.98	30.6	41.7
BR5	0.710001	0.000041	409	324	30.0	23.2	1.26	13.6	17.6
BR96	0.709255	0.000032	260	128	12.4	9.4	2.03	21.0	27.7
AFG2	0.723134	0.000035	456	281	26.9	20.3	1.62	17.0	22.5
AFB1	0.718859	0.000043	580	435	38.6	26.6	1.33	15.0	21.8
MADAP	0.705078	0.00005	2221	310	26.7	18.0	7.16	83.2	123
OL2	0.704218	0.000049	1612	963	91.0	68.0	1.67	17.7	23.7
OL3	0.704214	0.000030	1629	1005	97.0	73.0	1.62	16.8	22.3
NUAN	0.711770	0.000032	287	281	23.5	24.2	1.02	12.2	11.8

$^{87}\text{Sr}/^{86}\text{Sr}$ uncertainty from duplicate runs from the same dissolution.

Trace element data are from Table 2 and mass fractions are in units of $\mu\text{g g}^{-1}$.

scale. A total of fifty-five data points were measured in BR96 and the $\delta^{34}\text{S}$ 2s is 0.80‰, with a respective range of 2.0‰ (Figure 10c).

An additional data set (Session 5, Table 5, Figure 10d) was collected using seventy cycle isotope ratio collection to improve the 2s at the expense of analysis time, to see if $\Delta^{33}\text{S}$ could be detected in BR96. The 2s for $\delta^{34}\text{S}$ and $\delta^{33}\text{S}$ 2s improved slightly (Table 5) and we were able to reduce the external multiple analysis standard deviation of $\Delta^{33}\text{S}$ to the level required to identify a small MIF $\Delta^{33}\text{S} = -0.7 \pm 0.42\text{‰}$ (2s) in BR96. The apatite S isotopic compositions (Table 5) are not overly diagnostic of the source components, as $10^3\delta^{34}\text{S}$ ranges from 9–19. This range includes $10^3\delta^{34}\text{S}$ values from sedimentary, biogenic and volcanic sulfides, volcanic SO_2 , some sediments and granites, mantle derived anhydrite and seawater (Farquhar *et al.* 2000, Allègre 2008). So far, SIMS sulfur isotope measurements have not identified chemical matrix or crystallographic orientation effects (Economos *et al.* 2017, Hammerli *et al.* 2021). Our data is consistent with these conclusions. Individual measurement results for sulfur isotopes by SIMS are given in Table S2.

Sr isotope compositions

The TIMS $^{87}\text{Sr}/^{86}\text{Sr}$ ratios (Table 6) range from 0.704214 ± 0.000030 in OL3 to 0.723134 ± 0.000035 in AFG2. This range encompasses Sr isotopic compositions from mantle-derived rocks to felsic continental crust. Strontium mass fractions range from $260 \mu\text{g g}^{-1}$ in BR96 to $2221 \mu\text{g g}^{-1}$ in MADAP. BR2, BR5 and BR96, which are from the same locality have very similar $^{87}\text{Sr}/^{86}\text{Sr}$ ratios, respectively 0.709955 ± 0.000035 , $0.710001 \pm$

0.000041 and 0.709255 ± 0.000032 . The Otter Lake apatite, OL2 and OL3, have identical $^{87}\text{Sr}/^{86}\text{Sr}$ ratios within uncertainties, respectively 0.704218 ± 0.000049 and 0.704214 ± 0.000030 . These values are identical to the $^{87}\text{Sr}/^{86}\text{Sr}$ ratio of another Otter Lake apatite (Yang *et al.* 2014). The three Madagascar apatite, MADAP, AFG2 and AFB1, have distinctly different $^{87}\text{Sr}/^{86}\text{Sr}$ ratios, with respective values of 0.705078 ± 0.000050 , 0.723134 ± 0.000035 and 0.718859 ± 0.000043 . The variation of the Sr/Y, Sr/Er and Sr/Yb ratios, respectively 1.02 to 7.16, 13.6 to 83.2, and 11.8 to 123, of the apatite (Table 6), means these apatites will be helpful in the study of interferences on Sr isotope peaks during SIMS analysis, and for checking the validity of correction schemes used for *in situ* measurement of Sr isotopes in apatite (Gillespie *et al.* 2021, Jeon *et al.* 2021).

The pegmatite apatite OL2-OL4, BR2, BR5, BR96, AFB1, AFG2, SLAP and MADAP have REE patterns and contents that are consistent with evolved crustal sources. NUAN and the Otter Lake apatite have compositions that reflect a mix of evolved and primitive components. NUAN has low LREE and intermediate HREE contents, but a highly evolved $^{87}\text{Sr}/^{86}\text{Sr}$ ratio (0.71177). OL2 and OL3 have low $^{87}\text{Sr}/^{86}\text{Sr}$ (0.704214 and 0.704218, respectively), but high REE contents.

Common Pb correction of apatite U-Pb measurements

Comparison of the OL2 SIMS and ID-TIMS data provides an understanding of the importance of common Pb correction in apatite. Correction of the OL2 ID-TIMS U-Pb data with a Stacey and Kramers (1975) common Pb

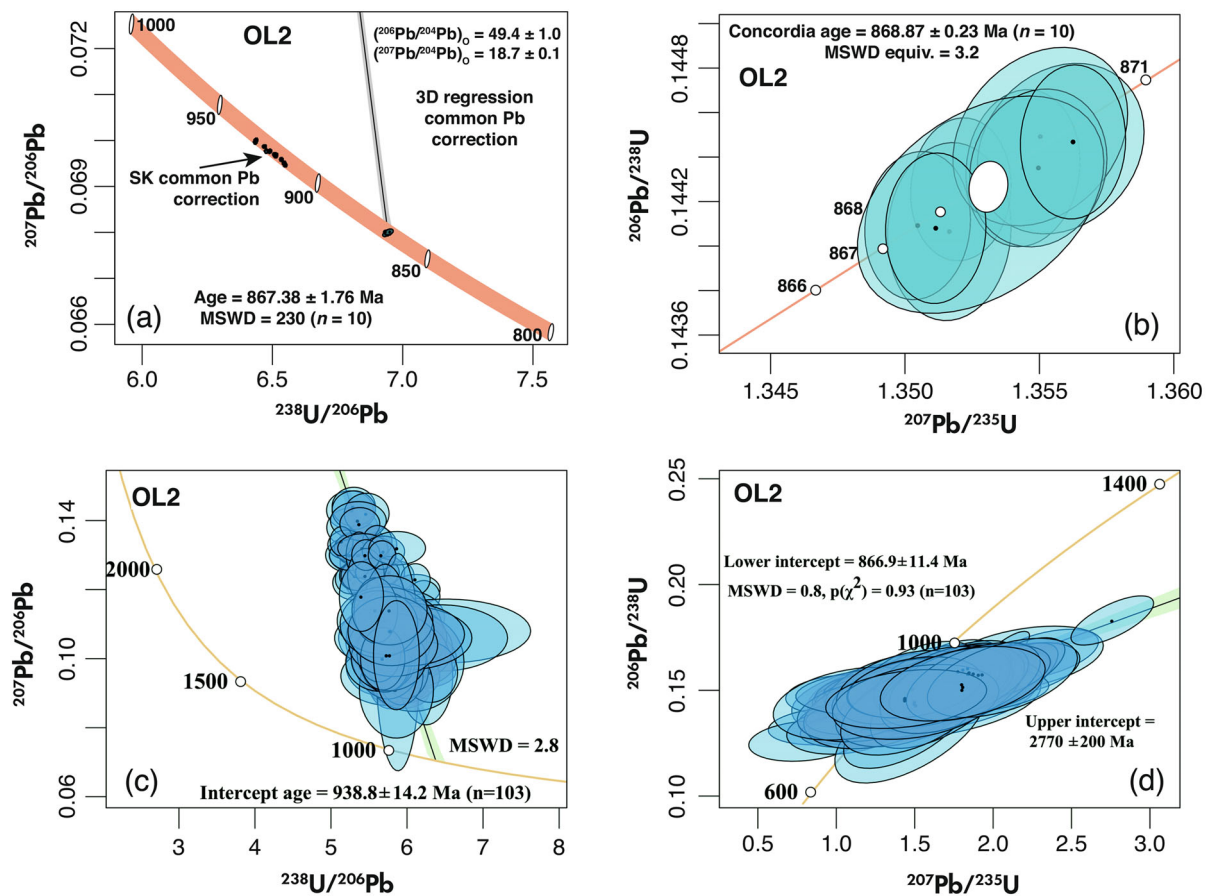


Figure 11. U-Pb data for OL2. (a) Tera-Wasserburg Concordia diagram showing, (1) the intersection of the regression line through the uncorrected ID-TIMS data with the Concordia at 867.38 ± 1.76 Ma, (2) the OL2 ID-TIMS U-Pb analyses corrected with the Stacey and Kramers (1975) common Pb composition at 868.87 ± 0.23 Ma, and (3) the OL2 ID-TIMS U-Pb analyses corrected with the Concordia constrained 3D common Pb composition. (b) The ID-TIMS Concordia constrained 3D data points for OL2 plotted on a Wetherill Concordia diagram, along with the calculated Concordia age. Ellipse uncertainties are 2s for ID-TIMS data. (c) The uncorrected SIMS U-Pb data for OL2 and the Tera-Wasserburg Concordia intercept age of 938.8 ± 14.2 Ma obtained by linear regression of the data. (d) SIMS data corrected with the Concordia constrained 3D common Pb composition plotted on a Wetherill Concordia diagram. Linear regression through the corrected data gives a Concordia intercept age of 866.9 ± 11.4 Ma. Ellipse uncertainties are 1s for SIMS data.

composition for an assumed age of 869 Ma gives scattered results, with the 10 TIMS analyses spreading along the Concordia between 910 and 930 Ma (Figure 11a). In contrast, if the correction for common Pb is based on a Concordia constrained 3D regression of the ID-TIMS data, the resultant points plot as a very tight group (Figure 11a) with an intercept age for OL2 of 867.38 ± 1.76 Ma (95% C.I.). The Concordia constrained common Pb composition is unusual and has $^{206}\text{Pb}/^{204}\text{Pb} = 49.4 \pm 1.0$, and $^{207}\text{Pb}/^{204}\text{Pb} = 18.7 \pm 0.1$. Figure 11b shows a magnified view of the ID-TIMS data corrected with this common Pb composition plotted on a Wetherill Concordia diagram. A

Concordia intercept age is calculated from the regressed points we get a value of 868.87 ± 0.23 Ma. Even though this age is for points that have been forced to be concordant, the MSWD of equivalence is still high, with a value of 3.2. This indicates that there is scatter of the OL2 ID-TIMS data in 3D that is beyond what is expected based on the uncertainty of the analyses.

The OL2 apatite uncorrected SHRIMP data plots as a loosely defined linear array that is above the Concordia curve in a Tera-Wasserburg Concordia diagram (Figure 11c). A linear regression of this data array gives a regression

intercept of 938.8 ± 14.2 Ma, with an MSWD of 2.8. Thus, a simple regression of the uncorrected SIMS data fails to give a meaningful age, as the intercept with the Concordia is 70 Ma older than the ID-TIMS age of OL2. The OL2 SHRIMP data, corrected with the Concordia constrained 3D regression common Pb (Figure 11d) is slightly discordant and exhibits a secondary alignment produced by a number of points that are under- or over-corrected for common Pb. A model 1 discordia fit to this SHRIMP OL2 common Pb corrected data gives an age of 866.9 ± 11.4 Ma (2s) as the lower intercept, which matches the TIMS value (Figure 11d).

It is obvious from the above examination of ID-TIMS and SHRIMP data for the OL2 apatite, that the age obtained is critically dependant on knowledge of the common Pb composition. The only time this statement can be ignored is when the apatite in question has a trivial amount of common Pb, or contains common Pb that matches Stacey and Kramers (1975) common Pb. For all the apatite we have analysed, the TIMS 3D Concordia constrained common Pb compositions do not match the Stacey and Kramers (1975) common Pb compositions at the apatite age (Table 4). The magnitude of the bias in the calculated age depends on the difference between the derived 3D common Pb composition and the Stacey and Kramers (1975) common Pb compositions, and the amount of common Pb measured during the analysis. OL2 is an extreme case and typically the age bias is 5–10 Ma, which may be considered a minor inaccuracy at 4 Ga, but a major issue in studies of Phanerozoic apatite. Our age for OL2 is identical to the intercept age for the Otter Lake apatite sample analysed by Xiang *et al.* (2021), when a common Pb correction is applied to the LA-ICP-MS data.

Conclusions

None of the apatite samples studied here are perfectly homogeneous. The five apatite reference samples analysed by ID-TIMS exhibit heterogeneity in Pb isotopes between individual chips, and the TIMS 3D Concordia constrained common Pb compositions do not match the Stacey and Kramers, (1975) model common Pb compositions at the apatite age. This results in significant offset in the calculated age that depends on the difference in the common Pb composition and the amount of common Pb. For OL2 this results in an error of ~70 Ma in the calculated age. AFG2 is the only apatite that produces a concordant, single age data set when the ID-TIMS data is corrected with a single common Pb composition. Similarly, there is minor

heterogeneity in trace elements by LA-ICP-MS and major elements by EPMA-WDS. Our data show that AFG2 and BR5 will be the best reference materials for U-Pb isotope measurement by SIMS, as the apatites have relatively high U, Th and $^{206}\text{Pb}/^{204}\text{Pb}$, and greater homogeneity than many naturally occurring apatite samples. AFB1 has exceptionally high Th and may be useful as a reference material for SIMS Th-Pb dating of apatite. The presence of variable amounts of common Pb, which itself shows some heterogeneity in composition, means that the apatites studied here cannot be used as single chip ID-TIMS U-Pb reference material. The faceted gem apatites, GR40 and SLAP, have the best homogeneity of trace elements and will be useful as reference materials for apatite trace element determination. Most of the apatite analysed for sulfur isotopes have good homogeneity and BR96 and SLAP will be useful for *in situ* sulfur isotope microanalysis of apatite. Our preliminary Sr isotope data cover a wide range of $^{87}\text{Sr}/^{86}\text{Sr}$ ratios, and when this is combined with the variation of Sr/Y, Sr/Er and Sr/Yb ratios, the best potential RMs for *in situ* SIMS Sr isotope measurement are MADAP and OL3. Chips of AFG2, BR5, GR40, SLAP, BR96, MADAP and OL3 can be obtained from AKK upon request.

Acknowledgements

We thank three anonymous reviewers for their constructive comments and suggestions, which improved the manuscript clarity and focus. This research was supported by NCRIS funding of the Large Geometry Ion Microprobe Facility and TIMS lab of the John de Laeter Centre, at Curtin University, the Australian Microscopy and Microanalysis Research Facility through Adelaide Microscopy at the University of Adelaide, and the CMCA at The University of Western Australia. US acknowledges on-going financial support of the Swiss National Science Foundation for the isotope laboratories at University of Geneva. JC and MS at Boise State University acknowledge the support of the NSF. Our thanks go to Boswel Wing at the University of Colorado for the provision of S isotope data during this project. THB is supported by McGill University, Montreal, Quebec, Canada. Open access publishing facilitated by Curtin University, as part of the Wiley - Curtin University agreement via the Council of Australian University Librarians.

Data availability statement

The data that support the findings of this study are available in the supplementary material of this article.

References

- Allègre C.J. (2008)**
Isotope geology. Cambridge University Press, (Cambridge), 512pp.
- Amelin Y. and Zaitsev A.N. (2002)**
Precise geochronology of phosphates and carbonates: The critical role of U-series disequilibrium in age interpretations. *Geochimica et Cosmochimica Acta*, 66, 2399–2419.
- Anders E. and Grevesse N. (1989)**
Abundances of the elements: Meteoritic and solar. *Geochimica et Cosmochimica Acta*, 53, 197–214.
- Antoine C., Bruand E., Guitreau M. and Devidal J.L. (2020)**
Understanding preservation of primary signatures in apatite by comparing matrix and zircon-hosted crystals from the Eoarchean Acasta Gneiss Complex (Canada). *Geochemistry Geophysics Geosystems*, 21, e2020GC008923.
- Ayers J.C. and Watson E.B. (1993)**
Apatite/fluid partitioning of rare-earth elements and strontium: Experimental results at 1.0 GPa and 1000 °C and application to models of fluid-rock interaction. *Chemical Geology*, 110, 299–314.
- Bao Z., Shi Y., Anderson J.L., Kennedy A., Ke Z., Gu X., Wang P., Che X., Kang Y., Sun H. and Wang C. (2022)**
Pb-Pb age of gabbroic lunar meteorite Northwest Africa 5000. LPSC, Abstract. The Woodlands, Texas. LPI Contribution No. 2678, id.1727.
- Barfod G.H., Krogstad E.J., Frei R. and Albarède F. (2005)**
Lu-Hf and Pb-Sr geochronology of apatites from Proterozoic terranes: A first look at Lu-Hf isotopic closure in metamorphic apatite. *Geochimica et Cosmochimica Acta*, 69, 1847–1859.
- Barrett T.J., Barnes J.J., Anand M., Franchi I.A., Greenwood R.C., Charlier B.L.A., Zhao X., Moynier F. and Grady M.M. (2019)**
Investigating magmatic processes in the early Solar System using the Cl isotopic systematics of eucrites. *Geochimica et Cosmochimica Acta*, 266, 582–597.
- Bellucci J.J., Nemchin A.A., Whitehouse M.J., Humayun M., Hewins R. and Zanda B. (2015)**
Pb-isotopic evidence for an early, enriched crust on Mars. *Earth and Planetary Science Letters*, 410, 34–41.
- Belousova E., Griffin W., O'Reilly S.Y. and Fisher N. (2002)**
Apatite as an indicator mineral for mineral exploration: Trace-element compositions and their relationship to host rock type. *Journal of Geochemical Exploration*, 76, 45–69.
- Bingen B., Demaiffe D. and Hertogen J. (1996)**
Redistribution of rare earth elements, thorium and uranium over accessory minerals in the course of amphibolite to granulite facies metamorphism: The role of apatite and monazite in orthogneisses from southwestern Norway. *Geochimica et Cosmochimica Acta*, 60, 1341–1354.
- Blake R.E., Chang S.J. and Lepland A. (2010)**
Phosphate oxygen isotopic evidence for a temperate and biologically active Archaean ocean. *Nature*, 464, 1029–1032.
- Bodorkos S., Bowring J. and Rayner N. (2020)**
Squid3: Next-generation data processing software for sensitive high resolution ion micro probe (SHRIMP). Geoscience Australia.
- Boehnke P., Bell E.A., Stephan T., Trappitsch R., Keller C.B., Pardo O.S., Davis A.M., Harrison T.M. and Pellin M.J. (2018)**
Potassic, high-silica Hadean crust. *Proceedings of the National Academy of Sciences*, 115, 6353–6356.
- Bowring J.F., McLean N.M. and Bowring S.A. (2011)**
Engineering cyber infrastructure for U-Pb geochronology. Tripoli and U-Pb_Redux. *Geochemistry Geophysics Geosystems*, 12.
- Boyce J., Tomlinson S., McCubbin F., Greenwood J. and Treiman A. (2014)**
The lunar apatite paradox. *Science*, 344, 400–402.
- Bright C.A., Cruse A.M., Lyons T.W., MacLeod K.G., Glascock M.D. and Ehington R.L. (2009)**
Seawater rare-earth element patterns preserved in apatite of Pennsylvanian conodonts? *Geochimica et Cosmochimica Acta*, 73, 1609–1624.
- Bruand E., Fowler M., Storey C. and Darling J. (2017)**
Apatite trace element and isotope applications to petrogenesis and provenance. *American Mineralogist*, 102, 75–84.
- Charlie B.L., Ginibre C., Morgan D., Nowell G.M., Pemson D.G., Davidson J.P. and Ottley C.J. (2006)**
Methods for the microsampling and high-precision analysis of strontium and rubidium isotopes at single crystal scale for petrological and geochronological applications. *Chemical Geology*, 232, 114–133.
- Chen M., Bagas L., Liao X., Zhang Z. and Li Q. (2019)**
Hydrothermal apatite SIMS Th-Pb dating: Constraints on the timing of low-temperature hydrothermal Au deposits in Nibao, SW China. *Lithos*, 324–325, 418–428.
- Chen W. and Simonetti A. (2013)**
In-situ determination of major and trace elements in calcite and apatite, and U-Pb ages of apatite from the Oka carbonatite complex: Insights into a complex crystallisation history. *Chemical Geology*, 353, 151–172.
- Chew D.M., Sylvester P.J. and Tubrett M.N. (2011)**
U-Pb and Th-Pb dating of apatite by LA-ICP-MS. *Chemical Geology*, 280, 200–216.



references

Cloué-Long J.C., Compston W., Roberts J. and Fanning C.M. (1995)

Two Carboniferous ages: A comparison of SHRIMP zircon dating with conventional zircon ages and $^{40}\text{Ar}/^{39}\text{Ar}$ analysis. In: Berggren W.A., Kent D.V., Aubrey M.P. and Hardenbol J. (eds), *Geochronology, time scales and global stratigraphic correlation*. Society for Sedimentary Geology Special Publication, 54, 3–21.

Compston W., Williams I. and Meyer C. (1984)

U-Pb geochronology of zircons from lunar breccia 73217 using a sensitive high mass-resolution ion microprobe. *Journal of Geophysical Research, Solid Earth*, 89, B525–B534.

Condon D., Schoene B., Bowring S., Parish R., McLean N., Noble S. and Crowley Q. (2007)

EARTHTIME: Isotopic tracers and optimized solutions for high-precision U-Pb ID-TIMS geochronology. AGU Fall Meeting Abstracts, V41E–06.

Cross A.J. and Williams I.S.E. (2018)

SHRIMP U-Pb-Th xenotime (YPO₄) geochronology: A novel approach for the correction of SIMS matrix effects. *Chemical Geology* 484, 81–108.

Davis W., Gall Q., Jefferson C. and Rainbird R. (2011)

Fluorapatite in the Paleoproterozoic Thelon Basin: Structural-stratigraphic context, *in-situ* ion microprobe U-Pb ages and fluid-flow history. *Bulletin*, 123, 1056–1073.

de Laeter J.R. and Kennedy A.K. (1998)

A double focusing mass spectrometer for geochronology. *International Journal of Mass Spectrometry*, 178, 43–50.

Decrée S., Cawthorn G., Deloué E., Mercadier J., Frimmel H. and Baelle J.M. (2020)

Unravelling the processes controlling apatite formation in the Phalaborwa Complex (South Africa) based on combined cathodoluminescence, LA-ICP-MS and *in-situ* O and Sr isotope analyses. *Contributions to Mineralogy and Petrology*, 175, 1–31.

Doucelance R., Bruand E., Matte S., Bosq C., Auclair D. and Gannoun A.M. (2020)

In-situ determination of Nd isotope ratios in apatite by LA-MC-ICP-MS: Challenges and limitations. *Chemical Geology*, 550, 119740.

Economos R., Boehnke P. and Burgisser A. (2017)

Sulfur isotopic zoning in apatite crystals: A new record of dynamic sulfur behavior in magmas. *Geochimica et Cosmochimica Acta*, 215, 387–403.

Edwards C.T., Saltzman M.R., Royer D.L. and Fike D.A. (2017)

Oxygenation as a driver of the Great Ordovician Biodiversification Event. *Nature Geoscience*, 10, 925–929.

Eiler J.M., Graham C. and Valley J.W. (1997)

SIMS analysis of oxygen isotopes, matrix effects in complex minerals and glasses. *Chemical Geology*, 138, 221–244.

Emo R.B., Smit M.A., Schmitt M., Kooijman E., Scherer E.E., Sprung P., Bleeker W. and Mezger K. (2018)

Evidence for evolved Hadean crust from Sr isotopes in apatite within Eoarchean zircon from the Acasta Gneiss Complex. *Geochimica et Cosmochimica Acta*, 235, 450–462.

Farquhar J., Bao H. and Thiemens M. (2000)

Atmospheric influence of Earth's earliest sulfur cycle. *Science*, 289, 756–758.

Farquhar J., Wing B.A., McKeegan K.D., Harris J.W., Cartigny P. and Thiemens M.H. (2002)

Mass-independent sulfur of inclusions in diamond and sulfur recycling on early Earth. *Science*, 298, 2369–2372.

Farquhar J. and Wing B.A. (2003)

Multiple sulfur isotopes and the evolution of the atmosphere. *Earth and Planetary Science Letters*, 213, 1–13.

Fisher C.M., Bauer A.M., Luo Y., Sarkar C., Hanchar J.M., Vervoort J.D., Tapster S.R., Horstwood M. and Pearson D.G. (2020)

Laser ablation split-stream analysis of the Sm-Nd and U-Pb isotope compositions of monazite, titanite, and apatite – Improvements, potential reference materials, and application to the Archean Saglek Block gneisses. *Chemical Geology*, 539, 119493.

Gall Q., Davis W.J., Lowe D.G. and Dabros Q. (2017)

Diagenetic apatite character and *in-situ* ion microprobe U-Pb age, Keeseville Formation, Potsdam Group, New York State. *Canadian Journal of Earth Sciences*, 54, 785–797.

Gerstenberger H., Haase G. and El Nour F.A. (1997)

The origin of strontium and the strontium isotope budget of the river Nile. *Isotopes in Environmental and Health Studies*, 33, 349–356.

Gillespie J., Nemchin A.A., Kinny P.D., Martin L., Aleshin M., Roberts M.P., Ireland T.R., Whitehouse M.J., Jeon H., Cavosie A.J. and Kirkland C.L. (2021)

Strontium isotope analysis of apatite via SIMS. *Chemical Geology*, 559, 119979.

Giuliani A., Fiorentini M.L., Martin L.A., Farquhar J., Phillips D., Griffin W.L. and LaFlamme C. (2016)

Sulfur isotope composition of metasomatised mantle xenoliths from the Bulfontein kimberlite (Kimberley, South Africa): Contribution from subducted sediments and the effect of sulfide alteration on S isotope systematics. *Earth and Planetary Science Letters*, 445, 114–124.

Gonçalves G., Lana C., Scholz R., Buick I. and Santos M. (2020)

Obtaining and maintaining the distribution of natural reference materials for U-Pb geochronology by LA-ICP-MS: Protocols and future perspectives. *Microscopy and Microanalysis*, 26, 3054–3055.

Grange M.L., Nemchin A.A., Pidgeon R.T., Timms N., Muhling J.R. and Kennedy A.K. (2009)

Thermal history recorded by the Apollo 17 impact melt breccia 73217. *Geochimica et Cosmochimica Acta*, 73, 3093–3107.

references

- Grange M., Nemchin A. and Pidgeon R. (2013)**
The effect of 1.9 and 1.4 Ga impact events on 4.3 Ga zircon and phosphate from an Apollo 15 melt breccia. *Journal of Geophysical Research, Planets*, 118, 2180–2197.
- Greenwood J.P., Blake R.E. and Coath C.D. (2003)**
Ion microprobe measurements of $^{18}\text{O}/^{16}\text{O}$ ratios of phosphate minerals in the Martian meteorites ALH84001 and Los Angeles. *Geochimica et Cosmochimica Acta*, 67, 2289–2298.
- Hammerli J., Greber N.D., Martin L., Bouvier A.S., Kemp A.L., Fiorentini M.L., Spangenberg J.E., Ueno Y. and Schaltegger U. (2021)**
Tracing sulfur sources in the crust via SIMS measurements of sulfur isotopes in apatite. *Chemical Geology*, 579, 120242.
- Hauri E.H., Saal A.E., Rutherford M.J. and Van Orman J.A. (2015)**
Water in the Moon's interior: Truth and consequences. *Earth and Planetary Science Letters*, 409, 252–264.
- Henrichs I.A., O'Sullivan G., Chew D.M., Mark C., Babechuk M.G., McKenna C. and Emo R. (2018)**
The trace element and U-Pb systematics of metamorphic apatite. *Chemical Geology*, 483, 218–238.
- Horstwood M., Evans J. and Montgomery J. (2008)**
Determination of Sr isotopes in calcium phosphates using laser ablation-inductively coupled plasma-mass spectrometry and their application to archaeological tooth enamel. *Geochimica et Cosmochimica Acta*, 72, 5659–5674.
- Ickert R.B., Hiess J., Williams I.S., Holden P., Ireland T.R., Lanc P., Schram N., Foster J.J. and Clement (2008)**
Determining high precision, in situ, oxygen isotope ratios with a SHRIMP II: Analyses of MPI-DING silicate-glass reference materials and zircon from contrasting granites. *Chemical Geology*, 257, 114–128.
- Ireland T.R. and Williams I.S. (2003)**
Considerations in zircon geochronology by SIMS. *Reviews in Mineralogy and Geochemistry*, 53, 215–241.
- Jaffey A., Flynn K., Glendenin L., Bentley W.T. and Essling A. (1971)**
Precision measurement of half-lives and specific activities of ^{235}U and ^{238}U . *Physical Review C*, 4, 1889.
- Jeon H. and Whitehouse M.J. (2021)**
A robust LG-SIMS method for Sr isotope determination in apatite across a wide Sr concentration range. *Geostandards and Geoanalytical Research*, 45, 325–340.
- Johnston D.T. (2011)**
Multiple sulfur isotopes and the evolution of Earth's surface sulfur cycle. *Earth-Science Reviews*, 106, 161–183.
- Kennedy A.K., Kamo S.L., Nasdala L. and Timms N.E. (2010)**
Grenville skarn titanite: Potential reference material for SIMS U–Th–Pb analysis. *The Canadian Mineralogist*, 48, 1423–1443.
- Kennedy A. (2011)**
New U-Th-Pb isotope reference material for SIMS. *Microscopy and Microanalysis*, 17, 836–837.
- Kennedy A., Crowley J., Schmitz M. and Wotzlaw J. (2012)**
SHRIMP apatite analysis and data reduction. 6th International SHRIMP Workshop, 68pp.
- Kennedy A.K., Wotzlaw J.-F., Schaltegger U., Crowley J.L. and Schmitz M. (2014)**
Eocene zircon reference material for microanalysis of U-Th-Pb isotopes and trace elements. *The Canadian Mineralogist*, 52, 409–421.
- Kita N., Huberty J., Kozdon R., Beard B. and Valley J. (2011)**
High-precision SIMS oxygen, sulfur and iron stable isotope analyses of geological materials: Accuracy, surface topography and crystal orientation. *Surface and Interface Analysis*, 43, 427–431.
- Kocsis L., Ulianov A., Mouflih M., Khaldoune F. and Gheerbrant E. (2021)**
Geochemical investigation of the taphonomy, stratigraphy, and palaeoecology of the mammals from the Ouled Abdoun Basin (Paleocene-Eocene of Morocco). *Palaeogeography, Palaeoclimatology, Palaeoecology*, 577, 110523.
- Krestianinov E., Amelin Y., Neymark L.A. and Aleinikov J.N. (2021)**
U-Pb systematics of uranium-rich apatite from Adirondacks: Inferences about regional geological and geochemical evolution, and evaluation of apatite reference materials for *in-situ* dating. *Chemical Geology*, 581, 120417.
- Rogh T. (1973)**
A low-contamination method for hydrothermal decomposition of zircon and extraction of U and Pb for isotopic age determinations. *Geochimica et Cosmochimica Acta*, 37, 485–494.
- Kusebauch C., John T., Whitehouse M.J. and Engvik A.K. (2015)**
Apatite as probe for the halogen composition of metamorphic fluids (Bamble Sector, SE Norway). *Contributions to Mineralogy and Petrology*, 170, 1–20.
- Le Houedec S., McCulloch M., Trotter J. and Rankenburg K. (2017)**
Conodont apatite $\delta^{88/86}\text{Sr}$ and $\delta^{44/40}\text{Ca}$ compositions and implications for the evolution of Palaeozoic to early Mesozoic seawater. *Chemical Geology*, 453, 55–65.
- Lev S., McLennan S. and Hanson G. (1999)**
Mineralogic controls on REE mobility during black-shale diagenesis. *Journal of Sedimentary Research*, 69, 1071–1082.



references

- Li Q.L., Li X.H., Wu F.Y., Yin Q.Z., Ye H.M., Liu Y., Tang G.Q. and Zhang C.L. (2012)**
In-situ SIMS U-Pb dating of Phanerozoic apatite with low U and high common Pb. *Gondwana Research*, 21, 745–756.
- Li W., Chakraborty S., Nagashima K. and Costa F. (2020)**
Multicomponent diffusion of F, Cl and OH in apatite with application to magma ascent rates. *Earth and Planetary Science Letters*, 550, 116545.
- Li Y., Li Q.L., Tang G.Q., Gargano A., Sharp Z., Pitawala A., Zhao L., Zhai M.G. and Li X.H. (2020)**
Eppawala-AP, Sri Lanka: An apatite reference material for high precision chlorine isotope analysis. *Atomic Spectroscopy*, 41, 51–56.
- Li Y., Tang G.Q., Liu Y., He S., Chen B., Li Q.L. and Li X.H. (2021)**
Revisiting apatite SIMS oxygen isotope analysis and Qinghu-AP reference material. *Chemical Geology*, 582, 120445.
- Ludwig K. (2009)**
SQUID 2: A user's manual. Berkeley Geochronology Center Special Publication, 5, 110pp.
- Ludwig K.R. (2003)**
User's manual for IsoPlot 3.0: A geochronological toolkit for Microsoft Excel. Berkeley Geochronology Center Special Publication, NN, 71pp.
- Malarkey J., Pearson D.G., Kjarsgaard B.A., Davidson J.P., Nowell G.M., Ottley C.J. and Stammer J. (2010)**
From source to crust: Tracing magmatic evolution in a kimberlite and a melilitite using microsample geochemistry. *Earth and Planetary Science Letters*, 299, 80–90.
- Marks M.A., Wenzel T., Whitehouse M.J., Loose M., Zack T., Barth M., Worgard L., Krasz V., Eby G.N., Stosnach H. and Mark G. (2012)**
The volatile inventory (F, Cl, Br, S, C) of magmatic apatite: An integrated analytical approach. *Chemical Geology*, 291, 241–255.
- McLean N.M., Bowring J.F. and Bowring S.A. (2011)**
An algorithm for U-Pb isotope dilution data reduction and uncertainty propagation. *Geochemistry Geophysics Geosystems*, 12.
- Nasdala L., Hofmeister W., Norberg N., Martinson J.M., Corfu F., Dörr W., Kamo S.L., Kennedy A.K., Kronz A., Reiners P.W. and Frei D. (2008)**
Zircon M257 – A homogeneous natural reference material for the ion microprobe U-Pb analysis of zircon. *Geostandards and Geoanalytical Research*, 32, 247–265.
- Nemchin A.A., Pidgeon R.T., Healy D., Grange M.L., Whitehouse M.J. and Vaughan J. (2009)**
The comparative behavior of apatite-zircon U-Pb systems in Apollo 14 breccias: Implications for the thermal history of the Fra Mauro Formation. *Meteoritics and Planetary Science*, 44, 1717–1734.

- Nixon A.L., Glorie S., Collins A.S., Whelan J.A., Reno B.L., Danišik M., Wade B.P. and Fraser G. (2021)**
Footprints of the Alice Springs Orogeny preserved in far northern Australia: An application of multi-kinetic thermochronology in the Pine Creek Orogen and Amhem Province. *Journal of the Geological Society of London*, 178, ijs2020-173.
- Norman M.D. and Nemchin A.A. (2014)**
A 4.2 billion year old impact basin on the Moon: U-Pb dating of zirconolite and apatite in lunar melt rock 67955. *Earth and Planetary Science Letters*, 388, 387–398.
- Pasek M.A., Hammeijer J.P., Buick R., Gull M. and Atlas Z. (2013)**
Evidence for reactive reduced phosphorus species in the early Archean ocean. *Proceedings of the National Academy of Sciences*, 110, 10089–10094.
- Paton C., Hellstrom J., Paul B., Woodhead J. and Hergt J. (2011)**
Iolite: Freeware for the visualisation and processing of mass spectrometric data. *Journal of Analytical Atomic Spectrometry*, 26, 2508–2518.
- Pearce N.J., Perkins W.T., Westgate J.A., Gorton M.P., Jackson S.E., Neal C.R. and Chenery S.P. (1997)**
A compilation of new and published major and trace element data for NIST SRM 610 and NIST SRM 612 glass reference materials. *Geostandards Newsletter: The Journal of Geostandards and Geoanalysis*, 21, 115–144.
- Raimondo T., Clark C., Hand M. and Faure K. (2011)**
Assessing the geochemical and tectonic impacts of fluid–rock interaction in mid-crustal shear zones: A case study from the intracontinental Alice Springs Orogen, central Australia. *Journal of Metamorphic Geology*, 29, 821–850.
- Ravindran A., Mezger K., Balakrishnan S., Kooijman E., Schmitt M. and Berndt J. (2020)**
Initial $^{87}\text{Sr}/^{86}\text{Sr}$ as a sensitive tracer of Archaean crust–mantle evolution: Constraints from igneous and sedimentary rocks in the western Dharwar Craton, India. *Precambrian Research*, 337, 105523.
- Sano Y., Terada K., Hidaka H., Yokoyama K. and Nutman A.P. (1999)**
Palaeoproterozoic thermal events recorded in the ~ 4.0 Ga Acasta gneiss, Canada: Evidence from SHRIMP U-Pb dating of apatite and zircon. *Geochimica et Cosmochimica Acta*, 63, 899–905.
- Sano Y., Koike M., Takahata N. and Terada K. (2016)**
Ion microprobe U-Pb dating of Zagami phosphates. 79th Annual Meeting of the Meteoritical Society, 79, 6083.
- Santos A.R., Agee C.B., McCubbin F.M., Shearer C.K., Burger P.V., Tartèse R. and Anand M. (2015)**
Petrology of igneous clasts in Northwest Africa 7034: Implications for the petrologic diversity of the Martian crust. *Geochimica et Cosmochimica Acta*, 157, 56–85.
- Schmitz M.D. and Schoene B. (2007)**
Derivation of isotope ratios, errors, and error correlations for U-Pb geochronology using ^{205}Pb - ^{235}U -(^{233}U)-spiked isotope dilution thermal ionisation mass spectrometric data. *Geochemistry Geophysics Geosystems*, 8.

references

Schoene B., Latkoczy C., Schaltegger U. and Günther D. (2010)

A new method integrating high-precision U-Pb geochronology with zircon trace element analysis (U-Pb TIMS-TEA). *Geochimica et Cosmochimica Acta*, **74**, 7144–7159.

Schaltegger U., Ovtcharova M., Gaynor S.P., Schoene B., Wotzlaw J.F., Davies J.F. and Chelle-Michou C. (2021)

Long-term repeatability and interlaboratory reproducibility of high-precision ID-TIMS U-Pb geochronology. *Journal of Analytical Atomic Spectrometry*, **36**, 1466–1477.

Silva C.B.S., Scholz R.C., Lana C.C., Madureira R.S., Gonçalves G.O., Albergaria G.H.C., Martins L.D.M. and Silva J.P.A. (2018)

Development of reference material for geochronology by LA-ICP-MS from apatite. *Proceedings of the 49th Brazilian Congress of Geology*, **7**.

Simpson A., Gilbert S., Tamblin R., Hand M., Spandler C., Gillespie J., Nixon A. and Glorie S. (2021)

In-situ Lu-Hf geochronology of garnet, apatite and xenotime by LA-ICP-MS/MS. *Chemical Geology*, **577**, 120299.

Smit K.V., Shirey S.B., Hauri E.H. and Stern R.A. (2019)

Sulfur isotopes in diamonds reveal differences in continent construction. *Science*, **364**, 383–385.

Stacey J. and Kramers J. (1975)

Approximation of terrestrial lead isotope evolution by a two-stage model. *Earth and Planetary Science Letters*, **26**, 207–221.

Stern R.A. and Berman R.G. (2001)

Monazite U-Pb and Th-Pb geochronology by ion microprobe, with an application to *in-situ* dating of an Archean metasedimentary rock. *Chemical Geology*, **172**, 113–30.

Stern R.A., Bodorkos S., Kamo S.L., Hickman A.H. and Corfu F. (2009)

Measurement of SIMS instrumental mass fractionation of Pb isotopes during zircon dating. *Geostandards and Geoanalytical Research*, **33**, 145–168.

Storey C., Smith M. and Jeffries T. (2007)

In-situ LA-ICP-MS U-Pb dating of metavolcanics of Norrbotten, Sweden: Records of extended geological histories in complex titanite grains. *Chemical Geology*, **240**, 163–181.

Sun Y., Wiedenbeck M., Joachimski M.M., Beier C., Kemner F. and Weinzierl C. (2016)

Chemical and oxygen isotope composition of gem-quality apatites: Implications for oxygen isotope reference materials for secondary ion mass spectrometry (SIMS). *Chemical Geology*, **440**, 164–178.

Tepper J.H. and Kuehner S.M. (1999)

Complex zoning in apatite from the Idaho batholith: A record of magma mixing and intracrystalline trace element diffusion. *American Mineralogist* **84**, 581–595.

Terada K. and Sano Y. (2012)

In-situ U-Pb dating of apatite by Hiroshima-SHRIMP. *Contributions to Earth and Planetary Science, Mass Spectrometry*, **1**, A0011–A0011.

Thode H., Monster J. and Dunford H. (1961)

Sulphur isotope geochemistry. *Geochimica et Cosmochimica Acta*, **25**, 159–174.

Thompson J., Meffre S., Maas R., Kamenetsky V., Kamenetsky M., Goemann K., Ehrig K. and Danyushevsky L. (2016)

Matrix effects in Pb/U measurements during LA-ICP-MS analysis of the mineral apatite. *Journal of Analytical Atomic Spectrometry*, **31**, 1206–1215.

Thomson S.N., Gehrels G.E., Ruiz J. and Buchwaldt R. (2012)

Routine low-damage apatite U-Pb dating using laser ablation-multicollector-ICP-MS. *Geochemistry Geophysics Geosystems*, **13**.

Trotter J.A., Williams I.S., Nicora A., Mazza M. and Rigo M. (2015)

Long-term cycles of Triassic climate change: A new $\delta^{18}\text{O}$ record from conodont apatite. *Earth and Planetary Science Letters*, **415**, 165–174.

Van Hoose A.E., Streck M.J. and Pallister J.S. (2010)

Apatite sulfur systematics and crystal population in the 1991 Pinatubo magmas. *AGU Fall Meeting Abstracts, American Geophysical Union*, V41B–2278.

Vermeesch P. (2018)

IsoplotR: A free and open toolbox for geochronology. *Geoscience Frontiers*, **9**, 1479–1493.

Williams I.S. (1998)

U–Th–Pb geochronology by ion microprobe. In: McKibben M.A. and Shanks W.C. (eds), *Applications of microanalytical techniques to understanding mineralizing processes*. *Reviews in Economic Geology*, 1–35.

Willigers B., Baker J., Krogstad E. and Peate D. (2002)

Precise and accurate *in-situ* Pb-Pb dating of apatite, monazite, and sphene by laser ablation multiple-collector ICP-MS. *Geochimica et Cosmochimica Acta*, **66**, 1051–1066.

Wotzlaw J.-F., Bindeman I.N., Schaltegger U., Brooks C.K. and Naslund H.R. (2012)

High-resolution insights into episodes of crystallisation, hydrothermal alteration and remelting in the Skaergaard intrusive complex. *Earth and Planetary Science Letters*, **355**, 199–212.

Wright J., Schrader H. and Holser W.T. (1987)

Paleoredox variations in ancient oceans recorded by rare earth elements in fossil apatite. *Geochimica et Cosmochimica Acta*, **51**, 631–644.



references

Wudarska A., Słaby E., Wiedenbeck M., Barnes J.D., Bonifacie M., Sturchio N.C., Bardoux G., Couffignal F., Glodny J., Heraty L. and John T. (2021)

Inter-laboratory characterisation of apatite reference materials for chlorine isotope analysis. *Geostandards and Geoanalytical Research*, 45, 121–142.

Wudarska A., Wiedenbeck M., Słaby E., Lempart-Drozd M., Harris C., Joachimski M.M. and Wilke F.D. (2022)

Inter-laboratory characterisation of apatite reference materials for oxygen isotope analysis and associated methodological considerations. *Geostandards and Geoanalytical Research*, 46, 277–306.

Xiang D., Zhang Z., Zack T., Chew D., Yang Y., Wu L. and Hogmalm J. (2021)

Apatite U-Pb dating with common Pb correction using LA-ICP-MS/MS. *Geostandards and Geoanalytical Research*, 45, 621–642.

Yamamoto S., Tanaka D., Sakata S., Obayashi H., Hirata T., Isozaki Y. and Komiya T. (2017)

The Hadean environment inferred from mineral inclusions within the oldest terrestrial zircons. *JpGU-AGU Joint Meeting*, BPT05-03.

Yang Q., Xia X.P., Zhang L., Zhang W., Zhang Y., Chen L., Yang Y. and He M. (2020)

Oxygen isotope homogeneity assessment for apatite U-Th-Pb geochronology reference materials. *Surface and Interface Analysis*, 52, 197–213.

Yang Y.H., Wu F.Y., Yang J.H., Chew D.M., Xie L.W., Chu Z.Y., Zhang Y.B. and Huang C. (2014)

Sr and Nd isotopic compositions of apatite reference materials used in U-Th-Pb geochronology. *Chemical Geology*, 385, 35–55.

Zhao X.-F., Zhou M.-F., Gao J.-F., Li X.-C. and Li J.-W. (2015)

In-situ Sr isotope analysis of apatite by LA-MC-ICP-MS: Constraints on the evolution of ore fluids of the Yinachang Fe-Cu-REE deposit, southwest China. *Mineralium Deposita*, 50, 871–884.

Žigaitė Ž. and Whitehouse M. (2014)

Stable oxygen isotopes of dental biomineral, differentiation at the intra- and inter-tissue level of modern shark teeth. *GFF*, 136, 337–340.

Supporting information

The following supporting information may be found in the online version of this article:

Table S1. SHRIMP U-Pb measurement results.

Table S2. CAMECA sulfur isotope measurement results.

Figure S6. Large scale, individual diagrams.

This material is available from: <http://onlinelibrary.wiley.com/doi/10.1111/ggr.12477/abstract> (This link will take you to the article abstract).